Computer Methods in Applied Mechanics and Engineering 419 (2024) 116628

Contents lists available at ScienceDirect

Comput. Methods Appl. Mech. Engrg.

journal homepage: www.elsevier.com/locate/cma

A scalable framework for multi-objective PDE-constrained design of building insulation under uncertainty

Jingye Tan [a], Danial Faghihi [b,*]

[a] Sibley School of Mechanical and Aerospace Engineering, Cornell University, Ithaca, NY, USA
[b] Department of Mechanical and Aerospace Engineering, University at Buffalo, Buffalo, NY, USA

ARTICLE INFO

Keywords:
Thermal insulation
Optimal design
PDE-constrained optimization
High-dimensional parameters
Uncertainty quantification

ABSTRACT

This paper introduces a scalable computational framework for optimal design under high-dimensional uncertainty, with application to thermal insulation components. The thermal and mechanical behaviors are described by continuum multi-phase models of porous materials governed by partial differential equations (PDEs), and the design parameter, material porosity, is an uncertain and spatially correlated field. After finite element discretization, these factors lead to a high-dimensional PDE-constrained optimization problem. The framework employs a risk-averse formulation that accounts for both the mean and variance of the design objectives. It incorporates two regularization techniques, the ℓ_0-norm and phase field functionals, implemented using continuation numerical schemes to promote spatial sparsity in the design parameters. To ensure efficiency, the framework utilizes a second-order Taylor approximation for the mean and variance and exploits the low-rank structure of the preconditioned Hessian of the design objective. This results in computational costs that are determined by the rank of preconditioned Hessian, remaining independent of the number of uncertain parameters. The accuracy, scalability with respect to the parameter dimension, and sparsity-promoting abilities of the framework are assessed through numerical examples involving various building insulation components.

1. Introduction

The quest for net-zero buildings in the battle against climate change has driven the exploration of novel materials for high-performance insulation components to enhance energy efficiency, reduce carbon footprint, and promote environmental sustainability. In particular, thermal breaks for building envelope insulation play a crucial role in interrupting heat flow paths and mitigating the adverse impact of thermal bridges at assembly interfaces [1,2]. Recently, silica aerogels have emerged as the most promising materials for next-generation thermal breaks due to their lightweight and ultralow thermal conductivity [3–6]. However, their limited mechanical strength due to high porosity hinders widespread adoption in construction [7–9]. Recent developments in additive manufacturing [10–12] have expanded the potential for precise material placement within components. For thermal breaks, for example, incorporating high porosity aerogel in certain regions provides exceptional insulation capabilities, while using low porosity aerogel in other areas enhances mechanical stability against environmental loads. To harness the potential of this technology, a reliable simulation-based design is crucial for optimizing material distribution and creating cost-effective components with superior insulation and mechanical performance.

* Corresponding author.
E-mail address: danialfa@buffalo.edu (D. Faghihi).

https://doi.org/10.1016/j.cma.2023.116628
Received 8 September 2023; Received in revised form 8 November 2023; Accepted 9 November 2023

Despite remarkable recent advancements in computational methods for designing materials with tailored performances, e.g., [13–23], the optimal design process involving partial differential equations (PDEs) of material properties remains confronted with formidable computational challenges. Firstly, uncertainty is inherent in the design process due to various factors, such as experimental data noise and model inadequacy during calibration and validation, errors in component fabrication, and randomness in external loads and environmental conditions. These uncertainties introduce variations in model and design parameters, leading to significant differences in the optimal design for different realizations. Secondly, the high dimensionality of the design problem, combined with the computational cost of solving possibly nonlinear PDEs for large-scale systems, poses another challenge. Accurate discretization of the forward model gives rise to a PDE-constrained optimization problem with high-dimensional design parameters, leading to computationally prohibitive solutions due to the so-called *curse of dimensionality*. The final challenge is achieving desirable design characteristics. For instance, a continuous spectrum of aerogel materials may render high-volume and cost-effective production of thermal breaks unfeasible. Therefore, it is crucial to incorporate appropriate regularizations in the optimization process to balance enforcing solution sparsity and achieving conflicting design objectives while accommodating uncertainty in the high-dimensional parameter spaces.

In recent years, the development of computational methods to handle uncertainty in PDE-constrained optimization under high-dimensional parameter space has gained significant attention, e.g., [24–42]. One class of risk-averse optimization involves formulating the cost functional to consider both the mean and variance of the objective, preventing undesired significant variations [30–32,40,43,44]. Other approaches include using conditional value-at-risk to measure the expectation of the objective exceeding a required level of risk aversion [36,45] and employing min–max optimization to seek the extreme values of the objective within the range of uncertain parameters [46]. However, these methods encounter significant computational challenges, particularly in high-dimensional parameter spaces, when evaluating the statistics of objectives, such as moments or conditional probabilities. Various approximations of statistical moments in the cost functional have been recently demonstrated in different PDE-constrained optimization problems. For instance, Doostan et al. [27] introduced an efficient topology optimization method that approximates the objective, constraints, and their gradients using a limited number of adjoint and forward solves per iteration. By employing a small number of random samples, this approach achieves substantial computational cost reduction compared to Monte Carlo methods An alternative class of approximations relies on the perturbation method, e.g., [47,48], utilizing truncated Taylor expansions to assess the moments of random variables and alleviate the computational demands of sampling methods. In their recent seminal works, Ghattas and co-workers [30–32,38] presented a scalable solution method for PDE-constrained optimization under high-dimensional uncertainty. Their approach leverages Taylor expansion of the mean and variance of the optimization objective with respect to the uncertain parameter field. Remarkably, by using the approximated objective directly or as a control variate for variance reduction, they achieve dimension-independent solutions and deliver several orders of magnitude in computational savings compared to Monte Carlo estimators. The linearization of the moments of the optimization objective using Taylor expansions has been previously incorporated into the robust design optimization framework by Doltsinis et al. [49,50] and applied to topology optimization by Lazarov et al. [51]. In a similar vein, Kriegesmann and co-workers [52–54] introduced a topology optimization method that utilizes the first-order second-moment method to compute the mean and standard deviation of the objective functions. They presented an efficient method to evaluate the variance gradient with one additional model evaluation [54]. Finally, Chen and Royset [55] conducted a comprehensive analysis of approximation-based algorithms for PDE-constrained optimization under uncertainty.

Expanding upon these earlier works, this study introduces a computational framework for risk-averse multi-objective PDE-constrained optimal design, with a particular emphasis on obtaining spatially sparse solutions. We implement this framework to design building insulation components, aiming to simultaneously enhance thermal performance while maintaining mechanical stability. In particular, the forward PDE consists of a two-phase thermo-mechanical continuum model of porous silica aerogel materials with model parameters determined from experimental data previously [56]. The design parameter is the spatial distribution of porosity over the domain of the insulation components, which includes uncertainty due to material variability and errors in the additive manufacturing process. The design parameter is a space-dependent field that, after finite element discretization, results in a high-dimensional optimal design problem under uncertainty. We adopt a risk-averse formulation that encompasses both the mean and variance of the thermal and mechanical design objectives, enabling us to attain the desired performance levels while mitigating the impact of uncertainty during optimization. Additionally, we introduce approximated ℓ_0-norm and phase field regularization functionals to promote spatial sparsity in the designed porosity field. To ensure the computational efficiency of our solution algorithm, we employ a second-order Taylor approximation for the design objective, alleviating the computational burden associated with Monte Carlo estimations of the mean and variance. Furthermore, we implement a gradient-based optimization method that exhibits dimension-independent convergence rates. These elements collectively contribute to the scalability of our framework for design under uncertainty, resulting in computational costs – measured in terms of the number of PDE solves – that remain independent by the dimensionality of the design parameters. We assess the accuracy, efficiency, and effectiveness of the sparsity-enforcing regularizations and the scalability of the framework through numerical examples featuring an L-shape insulation component and a thermal break within an envelope-column system.

The rest of the paper is organized as follows: Section 2 introduces the optimal design under uncertainty problem, using a general notation encompassing the PDE model, uncertain parameters, and the formulation of risk-averse optimization. Section 3 is dedicated to the computationally tractable methods, which involve the Taylor approximation of the design objective and randomized estimators to evaluate the resulting trace. Section 4 discusses the proposed regularization terms to enforce sparsity in the spatial distribution of the design parameters, along with the corresponding continuation numerical schemes. Section 5 describes the gradient-based optimization method and explains the computation of the gradient of the cost function concerning the design parameter. Section 6 adapts the design under uncertainty framework for building insulation components, covering the thermomechanical model and the formulation for multi-object optimization. Section 7 presents the numerical experiments on the optimal design of insulation components, followed by the conclusions and future works in Section 8.

2. PDE-constrained optimal design under uncertainty

In this section, we introduce the optimal design problem under uncertainty in an abstract setting, covering the representation of high-dimensional and spatially correlated uncertain parameters, as well as the formulation for mean–variance cost functional.

2.1. Forward model and design objectives

We denote the strong form of the (possibly nonlinear) PDE forward model in an abstract setting as,

$$\mathcal{R}(\mathbf{u}, m, d) = 0 \quad \text{in } \mathcal{V}', \tag{1}$$

which reads that given uncertain parameter $m \in \mathcal{M}$ and design parameter $d \in D$, find the state $\mathbf{u} \in \mathcal{U}$ such that minimizes the PDE residual operator $\mathcal{R}(\cdot)$ to zero in $\mathcal{V}'$. Here $\mathcal{U}$, $\mathcal{M}$ and D denote infinite-dimensional Hilbert space and $\mathcal{V}'$ the dual space. The weak form is then represented as,

$$r(\mathbf{u}, \mathbf{v}, m, d) := {}_{\mathcal{V}}\langle \mathbf{v}, \mathcal{R}(\mathbf{u}, m, d)\rangle_{\mathcal{V}'} = 0 \quad \forall \mathbf{v} \in \mathcal{V} \tag{2}$$

where $\mathbf{v}$ is the adjoint variables and ${}_{\mathcal{V}}\langle\cdot,\cdot\rangle_{\mathcal{V}'}$ represent the duality pairing between the $\mathcal{V}$ and $\mathcal{V}'$. The design objective is a general real-valued functional, denoted as Q, which not only depends on the state solution $\mathbf{u}$, but also explicitly depends on both the uncertain parameter m and the design parameter d, i.e., $Q(\mathbf{u}, d, m)$.

2.2. Uncertain parameter

We assume that the uncertain parameter m has a mean value of $\bar{m}$ and a covariance structure denoted as $\mathcal{C}$, that may, in general, be finite or infinite-dimensional within the proposed design under uncertainty framework. In particular, to address spatially correlated uncertainty, we consider $m(\mathbf{x})$ as a Gaussian random field using the Matérn kernel $\mathcal{C} = \mathcal{A}^{-2}$ [57], such that, the action of the operator $\mathcal{A}$ in the Sobolev space of functions with derivatives in $L^2(\Omega)$ on m is

$$\mathcal{A}\, m = \begin{cases} \gamma\, \nabla \cdot (\boldsymbol{\Theta}\, \nabla m) + \delta\, m & \text{in} \quad \Omega \\ (\boldsymbol{\Theta}\, \nabla m) \cdot \mathbf{n} + \frac{\sqrt{\delta\,\gamma}}{1.42}\, m & \text{on} \quad \Gamma. \end{cases} \tag{3}$$

In (3), γ and δ control the variance $\sigma^2 = 1/4\pi\,\delta\,\gamma$ and spatial correlation length $L_c = \sqrt{8\gamma/\delta}$, and ∇ and $\nabla\cdot$ are the gradient and divergence operators, respectively. The constant Robin coefficient $\sqrt{\delta\gamma}/1.42$ is employed to minimize boundary artifacts, following the approach in [58]. For a more advanced approach that involves a variable Robin coefficient determined through optimizations, we refer readers to [59]. Moreover, $\boldsymbol{\Theta}$ is a symmetric positive definite two-dimensional anisotropic tensor

$$\boldsymbol{\Theta} = \begin{bmatrix} \vartheta_x \sin^2(\alpha) + \vartheta_y \cos^2(\alpha) & (\vartheta_x - \vartheta_y)\sin(\alpha)\cos(\alpha) \\ (\vartheta_x - \vartheta_y)\sin(\alpha)\cos(\alpha) & \vartheta_x \cos^2(\alpha) + \vartheta_y \sin^2(\alpha) \end{bmatrix}, \tag{4}$$

where α is the angle between the magnitudes ϑ_x and ϑ_y in x and y directions, respectively.

2.3. Optimal design under uncertainty

Due to the explicit dependency of the design objective on the uncertainty parameter, Q is inherently a random variable. Extending the mean–variance optimization approach, e.g., [30,31], the cost functional for the proposed optimal design is expressed as,

$$\mathcal{J}(d) = \mathbb{E}[Q(\mathbf{u}, d, m)] + \beta_V\, \mathbb{V}[Q(\mathbf{u}, d, m)] + \beta_R\, R(d). \tag{5}$$

Here, $\mathbb{E}[\cdot]$ and $\mathbb{V}[\cdot]$ represent the mean and variance, and $R(d)$ is a regularization term. The weights β_V and β_R govern the relative importance of the variance of the design objective and the regularization term in relation to the means of the design objective. Accordingly, we can formulate the risk-averse PDE-constrained optimal design under uncertainty as,

$$\begin{aligned} d_{\text{opt}}(\mathbf{x}) = \underset{d\in[0,1]}{\text{argmin}} \quad & \mathcal{J}(d). \\ \text{subjected to} \quad & r(\mathbf{u}, \mathbf{v}, m, d) = 0. \end{aligned} \tag{6}$$

A common approach to compute the mean and variance terms in (5) is the sample average approximation for N_{mc} samples,

$$\mathbb{E}[Q] \approx \frac{1}{N_{mc}} \sum_{i=1}^{N_{mc}} Q(m^{(i)}), \tag{7}$$

$$\mathbb{V}[Q] \approx \Big(\frac{1}{N_{mc}} \sum_{i=1}^{N_{mc}} Q^2(m^{(i)})\Big) - \Big(\frac{1}{N_{mc}} \sum_{i=1}^{N_{mc}} Q(m^{(i)})\Big)^2, \tag{8}$$

where $\{m^{(i)}\}_{i=1}^{N_{mc}}$ are independent and identically distributed (i.i.d) random samples from the uncertain and spatially correlated parameter defined in Section 2.2. However, the Monte Carlo method exhibits a convergence rate of $\mathcal{O}\big(\frac{1}{\sqrt{N_{mc}}}\big)$, which requires a considerable number of PDE model evaluations to compute the cost functional (5) accurately, leading to computationally prohibitive optimization under uncertainty problem.

3. Taylor approximation of the design objective

In this section, we present a computationally tractable approach by approximating the mean and variance of the design objective by means of low-order Taylor expansion [30,31,51]. The Taylor approximation of Q at the mean of the uncertain parameter $\bar{m}$ truncated with L terms is,

$$T_L Q(m) = \sum_{l=0}^{L} \partial_m^l Q(\bar{m})\,(m-\bar{m})^l, \tag{9}$$

where $\partial_m^l Q(\bar{m})$ is the lth order tensor derivative, assumed to be sufficiently smooth and Fréchet differentiable with respect to the uncertain parameter Choosing $L = 2$, we obtain the quadratic Taylor approximation in the form

$$T_2 Q(m) = \bar{Q} + \left\langle \bar{Q}^m,\, m-\bar{m} \right\rangle + \frac{1}{2}\left\langle \bar{Q}^{mm}\,(m-\bar{m}),\, m-\bar{m} \right\rangle. \tag{10}$$

where $\bar{Q}$, $\bar{Q}^m$, and $\bar{Q}^{mm}$ represent the design objective and its gradient and Hessian with respect to m, respectively, all evaluated at the mean $\bar{m}$. In the above relation, the symbol $\langle \cdot,\cdot \rangle$ denotes the inner product. The closed-form expression for the expectation of the approximated design objective in (10) can be derived, taking into account $\mathbb{E}[\bar{Q}] = \bar{Q}$, $\mathbb{E}[\left\langle \bar{Q}^m,\, m-\bar{m} \right\rangle] = 0$, and Lemma 1 of [60], as the following expression:

$$\mathbb{E}[T_2 Q(m)] = \bar{Q} + \frac{1}{2}\mathrm{tr}\left(\bar{\mathcal{H}}_c\right), \tag{11}$$

where $\bar{\mathcal{H}}_c = \mathcal{C}\,\bar{Q}^{mm}$ denotes the covariance preconditioned Hessian computed at the mean of m and $\mathrm{tr}(\cdot)$ is trace operator. Moreover, noting that variance is invariant with respect to its translation, one can write,

$$\mathbb{E}[(T_2 Q(m) - \bar{Q})^2] = \mathbb{E}[(\left\langle \bar{Q}^m,\, m-\bar{m} \right\rangle + \frac{1}{2}\left\langle \bar{Q}^{mm}(m-\bar{m}),\, m-\bar{m} \right\rangle)^2], \tag{12}$$

which, after expansion, each term can be expressed as

$$\begin{aligned} \mathbb{E}[(\left\langle \bar{Q}^m,\, m-\bar{m} \right\rangle)^2] &= \left\langle \bar{Q}^m, \mathcal{C}\,\bar{Q}^m \right\rangle, \\ \mathbb{E}[(\left\langle \bar{Q}^{mm}(m-\bar{m}),\, m-\bar{m} \right\rangle)^2] &= \mathrm{tr}(\bar{\mathcal{H}}_c)^2 + 2\,\mathrm{tr}((\bar{\mathcal{H}}_c)^2), \\ \mathbb{E}[\left\langle \bar{Q}^m,\, m-\bar{m} \right\rangle \left\langle \bar{Q}^{mm}(m-\bar{m}),\, m-\bar{m} \right\rangle] &= 0. \end{aligned} \tag{13}$$

Furthermore, the square of the first moment of $T_2 Q(m) - \bar{Q}$ can be written as,

$$\left(\mathbb{E}[T_2 Q(m) - \bar{Q}]\right)^2 = \left(\mathbb{E}[T_2 Q(m)] - \mathbb{E}[\bar{Q}]\right)^2 = \frac{1}{4}\left(\mathrm{tr}\left(\bar{\mathcal{H}}_c\right)\right)^2. \tag{14}$$

From (13) and (14), the variance of the quadratic Taylor approximation of Q in (10) is obtained as,

$$\mathbb{V}[T_2 Q(m)] = \mathbb{V}[T_2 Q(m) - \bar{Q}] = \left\langle \bar{Q}^m, \mathcal{C}\,\bar{Q}^m \right\rangle + \frac{1}{2}\mathrm{tr}((\bar{\mathcal{H}}_c)^2). \tag{15}$$

Consequently, the mean and variance of the design objective in (5) can be replaced by their corresponding Taylor approximations in (11) and (15), respectively, leading to the quadratically approximated cost function as

$$\mathcal{J}_{\mathrm{quad}}(d) = \bar{Q} + \frac{1}{2}\mathrm{tr}\left(\bar{\mathcal{H}}_c\right) + \beta_V \left(\left\langle \bar{Q}^m, \mathcal{C}\,\bar{Q}^m \right\rangle + \frac{1}{2}\mathrm{tr}((\bar{\mathcal{H}}_c)^2) \right) + \beta_R\, R(d). \tag{16}$$

In upcoming sections, we present the Lagrangian formalism to derive the m-gradient and m-Hessian, representing the gradient and Hessian of Q with respect to m. We also introduce an efficient method for evaluating the covariance preconditioned Hessian, $\bar{\mathcal{H}}_c$.

3.1. Gradient and hessian of design objective with respect to the uncertain parameter

The Lagrangian functional, considering the adjoint variable $\mathbf{v}$ as the Lagrange multiplier associated with the state equation, is defined as,

$$\mathcal{L}(\mathbf{u}, \mathbf{v}, m, d) = Q(\mathbf{u}, d, m) + r(\mathbf{u}, \mathbf{v}, m, d), \tag{17}$$

where $r(\mathbf{u}, \mathbf{v}, m, d)$ is the weak form in (2). By imposing the condition that the first-order variation of the Lagrangian functional at $\bar{m}$ with respect to the adjoint variable $\mathbf{v}$ and the state variable $\mathbf{u}$ is equal to zero, we obtain, the state problem: *Find* $\mathbf{u} \in \mathcal{U}$*, such that*

$$\langle \tilde{\mathbf{v}}, \partial_{\mathbf{v}} \bar{r} \rangle = 0, \quad \forall \tilde{\mathbf{v}} \in \mathcal{V}, \tag{18}$$

and adjoint problem: *Find* $\mathbf{v} \in \mathcal{V}$*, such that*

$$\langle \tilde{\mathbf{u}}, \partial_{\mathbf{u}} \bar{r} \rangle = -\langle \tilde{\mathbf{u}}, \partial_{\mathbf{u}} \bar{Q} \rangle, \quad \forall \tilde{\mathbf{u}} \in \mathcal{U}. \tag{19}$$

In the above relations, $\bar{(\cdot)}$ denotes the quantities computed at the mean of the uncertain parameter, e.g., $\bar{r} = r(\mathbf{u}, \mathbf{v}, \bar{m}, d)$, and $\tilde{(\cdot)}$ indicates directional variables. The gradient of Q at $\bar{m}$ acting in the direction $\tilde{m} = m - \bar{m}$ is then given by,

$$\langle \tilde{m}, \bar{Q}^m \rangle = \langle \tilde{m}, \partial_m \bar{r} \rangle. \tag{20}$$

Thus, evaluating m-gradient in (20) requires the solution of state problem (18) for $\mathbf{u}$ and the adjoint problem (19) for $\mathbf{v}$.

To solve for the m-Hessian, we consider a meta-Lagrangian functional with incremental state $\hat{\mathbf{u}}$ and adjoint $\hat{\mathbf{v}}$

$$\mathcal{L}^H(\mathbf{u},\mathbf{v},m,d;\hat{\mathbf{u}},\hat{\mathbf{v}},\hat{m}) = \langle \hat{m}, \partial_m \bar{r}\rangle + \langle \hat{\mathbf{v}}, \partial_{\mathbf{v}} \bar{r}\rangle + \langle \hat{\mathbf{u}}, \partial_{\mathbf{u}} \bar{r} + \partial_{\mathbf{u}} \bar{Q}\rangle \tag{21}$$

where the terms on the right-hand side are m-gradient, state, and adjoint problems, respectively. Repeating the similar process of vanishing the first variation of the Lagrangian functional with respect to adjoint and state, we obtain the incremental state problem: *Find* $\hat{\mathbf{u}} \in \mathcal{U}$*, such that*

$$\langle \tilde{\mathbf{v}}, \partial_{\mathbf{vu}} \bar{r}\, \hat{\mathbf{u}}\rangle = -\langle \tilde{\mathbf{v}}, \partial_{\mathbf{v}m} \bar{r}\, \hat{m}\rangle, \quad \forall \tilde{\mathbf{v}} \in \mathcal{V}, \tag{22}$$

and the incremental adjoint problem: *Find* $\hat{\mathbf{v}} \in \mathcal{V}$*, such that*

$$\langle \tilde{\mathbf{u}}, \partial_{\mathbf{uv}} \bar{r}\, \hat{\mathbf{v}}\rangle = -\langle \tilde{\mathbf{u}}, \partial_{\mathbf{uu}} \bar{r}\, \hat{\mathbf{u}} + \partial_{\mathbf{uu}} \bar{Q}\, \hat{\mathbf{u}} + \partial_{\mathbf{u}m} \bar{r}\, \hat{m} + \partial_{\mathbf{u}m} \bar{Q}\, \hat{m}\rangle, \quad \forall \tilde{\mathbf{u}} \in \mathcal{U}. \tag{23}$$

By taking the variation of $\mathcal{L}^H$ with respect to m as zero, the Hessian of Q acting on $\hat{m}$ is computed as,

$$\langle \tilde{m}, \bar{Q}^{mm}\, \hat{m}\rangle = \langle \tilde{m}, \partial_{m\mathbf{v}} \bar{r}\, \hat{\mathbf{v}} + \partial_{m\mathbf{u}} \bar{r}\, \hat{\mathbf{u}} + \partial_{mm} \bar{r}\, \hat{m} + \partial_{m\mathbf{u}} \bar{Q}\, \hat{\mathbf{u}} + \partial_{mm} \bar{Q}\, \hat{m}\rangle. \tag{24}$$

We should note that the last term on the right-hand side of (23) and the last two terms on the right-hand side of (24) are included because we account for the explicit dependence of the design objective $Q(\mathbf{u}, d, m)$ on the design and uncertain parameters in this study. As a result, evaluating the m-Hessian acting on $\hat{m}$ in (24) requires the solution of the incremental state problem (22) for $\hat{\mathbf{u}}$ and the incremental adjoint problem (23) for $\hat{\mathbf{v}}$. For an overview of the steps in computing the m-gradient and m-Hessian, we direct interested readers to Algorithms 1 and 2 in [61].

3.2. Randomized trace estimator

The quadratic approximations for the mean (11) and variance (15) of the design objectives depend on the trace of the covariance preconditioned Hessian $\bar{\mathcal{H}}c$, which is typically a large dense matrix. A common approach to obtain the trace is through the Monte Carlo method, where the action of the Hessian on a number of random directions sampled from a Gaussian distribution is computed [30]. Nevertheless, even adhering to lower bounds on the required number of samples for attaining accurate trace approximations, as discussed in [62], entails substantial values (e.g., 10^6 samples are necessary to guarantee a probabilistic error bound of 10^{-3}). As a consequence of the substantial number of samples needed at each optimization iteration, this approach is computationally prohibitive for the design under uncertainty problem considered in this work. Here, we employ a randomized approximated eigen-decomposition to estimate the trace and trace-squared using the dominant eigenvalues $\{\lambda_n\}_{n=1}^{N_{\text{eig}}}$ of the covariance-preconditioned Hessian $\bar{\mathcal{H}}_c$, expressed as,

$$\operatorname{tr}\left(\bar{\mathcal{H}}_c\right) \approx \sum_{n\geq 1}^{N_{\text{eig}}} \lambda_n, \quad \operatorname{tr}\left(\bar{\mathcal{H}}_c^2\right) \approx \sum_{n\geq 1}^{N_{\text{eig}}} \lambda_n^2. \tag{25}$$

The above forms of trace estimators are justified by the symmetric positive definite property of the operator $\mathcal{H}_c$. It is noteworthy that the value of N_{eig} is invariant to the parameter dimension and in many problems, e.g., [63–66] it tends to be small when the covariance-preconditioned Hessian is low-rank or when its eigenvalues decay rapidly (see the numerical results of Section 7). The eigenvalues λ_n are obtained by solving the following generalized eigenvalue problem,

$$\left\langle \zeta, \bar{Q}^{mm}\, \psi_j \right\rangle = \lambda_j \left\langle \zeta, \mathcal{C}^{-1} \psi_j \right\rangle, \quad \forall \zeta \in \mathcal{M}, \quad j = 1, \ldots, N_{\text{eig}} \tag{26}$$

where the eigenvectors ψ_j exhibit orthonormality with $\mathcal{C}^{-1}$, $\left\langle \psi_i, \mathcal{C}^{-1}\psi_j \right\rangle = \delta_{ij}, i, j = 1, \ldots, N_{\text{eig}}$ and δ_{ij} denotes the Kronecker delta function. By an n-degree finite element discretization, (26) is recast into a matrix form as $\mathbf{A}\,\boldsymbol{\psi} = \lambda\, \mathbf{B}\,\boldsymbol{\psi}$ where $\mathbf{A}$ and $\mathbf{B}$ are n-by-n symmetric matrices, $\mathbf{B}$ is positive definite, and $\boldsymbol{\psi}$ represents a vector of size n. To solve the resulting eigenproblem, we employ a double-pass randomized algorithm [67], outlined in Algorithm 1.

Algorithm 1: Double-pass randomized algorithm

Input : Matrices $\mathbf{A}, \mathbf{B} \in \mathbb{R}^{n\times n}$ stem from finite element discretization, number of eigenpairs requested N_{eig}, oversampling factor N_{o}

Output: Eigenpairs (λ_j, ψ_j), $j = 1, ..., N_{\text{eig}}$

1 Generate a realization of a Gaussian random matrix $\mathbf{G} \in \mathbb{R}^{n\times(N_{\text{eig}}+N_{\text{o}})}$
2 Compute range $\mathbf{Y} = \mathbf{B}^{-1}(\mathbf{A}\,\mathbf{G})$
3 Compute QR-factorization $\mathbf{Y} = \mathbf{Q}\,\mathbf{R}$ such that $\mathbf{Q}^T\mathbf{B}\,\mathbf{Q} = \mathbf{I}_{N_{\text{eig}}+N_{\text{o}}}$
4 Compute $\mathbf{Q}^T\mathbf{A}\,\mathbf{Q}$
5 Compute eigenvalue decomposition $\mathbf{Q}^T\mathbf{A}\,\mathbf{Q} = \mathbf{S}\,\boldsymbol{\Lambda}\,\mathbf{S}^T$
6 Obtain the eigenpairs via $\lambda_j = \boldsymbol{\Lambda}[j,j]$, $\psi_j = \mathbf{Q}\,\mathbf{S}[:,j]$, $j = 1, ..., N_{\text{eig}}$.

4. Sparsity-enforcing regularizations and continuation schemes

The final aspect of the design problem involves selecting an appropriate regularization term $R(d)$ in (5). In Section 6, we will discuss the practical requirements of the problem, which include the need for a spatially sparse distribution of the design parameter, ideally comprising two materials with different porosities and a controlled interface thickness. The choice of regularization plays a critical role in this context and represents a significant contribution of the proposed design under uncertainty framework. We propose two sparsity-enforcing regularizations based on the ℓ_0-norm and double-well functions of the design parameter.

4.1. ℓ_0-Norm regularization

The ℓ_0-norm regularization has been utilized in discrete optimization problems, such as neural network pruning to encourage weights to become zero during training [68] and determining optimal sensor placement from a finite set of candidate locations in optimal experimental design problems [29]. For designing the spatial distribution of porosity within the domain, we define the ℓ_0-norm as the area of the non-zero regions in the design parameter field. However, this definition results in a non-convex function with a singularity near the origin ($d = 0$). Accordingly, we propose an approximated ℓ_0-norm in the regularization term for our problem as,

$$\beta_R\, R_0(d) = \beta_{\text{tik}} \int_\Omega |\nabla d|^2 \,\mathrm{d}\Omega + \int_\Omega f_{\epsilon_0}(d)\,\mathrm{d}\Omega, \tag{27}$$

where the first term is the Tikhonov regularization function, and f_{ϵ_0} is a continuously differentiable approximation of the ℓ_0-norm [29],

$$f_{\epsilon_0}(d) = \begin{cases} d/\epsilon_0, & d \in [0, \epsilon_0/2] \\ p_3(d, \epsilon_0), & d \in (\epsilon_0/2, 2\epsilon_0) \\ 1, & d \in (2\epsilon_0, 1]. \end{cases} \tag{28}$$

In the above equation, $p_3(d, \epsilon_0)$ is a third-order polynomial in terms of d, and $\epsilon_0 \in (0, 0.5]$ acts as a hyperparameter controlling the approximation accuracy of $f_{\epsilon_0}(d)$ to the ℓ_0-norm (see Fig. 1(a)). To ensure that $f_{\epsilon_0}(d)$ is continuously differentiable for $d \in [0, 1]$, we uniquely determine $p_3(d, \epsilon_0)$ based on the value of the hyperparameter ϵ_0. Specifically, we consider the polynomial in the form $p_3(d, \epsilon_0) = a_3\, d^3 + a_2\, d^2 + a_1\, d + a_0$, where $a_i(\epsilon_0)$ are the polynomial coefficients. To determine these coefficients, we impose certain conditions, including the polynomial p_3 must pass through the points $(\frac{\epsilon_0}{2}, \frac{1}{2})$ and $(2\epsilon_0, 1)$, and the derivatives at the left and right sides of $f_{\epsilon_0}(d = \frac{\epsilon_0}{2})$ and $f_{\epsilon_0}(d = 2\epsilon_0)$ should be equal. These conditions form a system of four equations that allow us to compute the polynomial coefficients.

4.2. Phase field regularization

Taking inspiration from the Ginzburg–Landau free energy functional used to model phase transition phenomena in binary systems, e.g., [69–71], we propose a phase field regularization with the following form,

$$\beta_V\, R_{\text{p}}(d) = \int_\Omega \left(\beta_{\text{tik}} |\nabla d|^2 + \beta_{\text{well}}\, W(d) \right) \mathrm{d}\Omega. \tag{29}$$

The first term of (29) corresponds to the Tikhonov regularization, while the second term consists of a double well function $W(d)$ with global minima at $d = 0$ and $d = 1$ and the parameter β_{well} serves to reinforce sparsity. Following [72], we propose the following second derivative double-well function $W(d)$ with respect to d,

$$W^{dd}(d) = \left(2\,(2d-1)^2\right) + \epsilon_w \left((2d-1)^2 - 1\right), \tag{30}$$

that decomposes the second derivative into a strictly positive term and a remainder term that may take non-positive values. The hyperparameter $\epsilon_w \in [0, 1]$ scales the second term in (30), thereby transforming it from a single well (at $\epsilon_w = 0$) to a full double well (at $\epsilon_w = 1$) located at $d = 0$ and $d = 1$, as depicted in Fig. 1(b).

It is worth acknowledging that phase field-based approaches have been an attractive approach in topology optimization methods, e.g., [73–75]. In these methods, the density function, which characterizes the material presence or absence, evolves using the modified Allen–Cahn differential equations [76,77]. However, our approach exploits the structure of the free energy function of phase-field models as a regularization term that obviates the need to solve additional time-dependent PDE. In parallel, the mathematical analysis of the resulting optimization problem, including rigorous derivation of minimizers and optimality conditions, is recently presented in [78].

4.3. Continuation numerical schemes

To handle potential multiple local minima arising from the non-convex regularization functions (27) and (29), we employ continuation numerical schemes with respect to the hyperparameters ϵ_0 and ϵ_w. The continuation procedure involves solving the optimization problem (6) with an evolving regularization function, utilizing a decreasing sequence of hyperparameters $\{\epsilon_0^{(i)} = (\frac{1}{2})^i\}_{i=1}^K$ for ℓ_0-norm regularization and an increasing sequence of $\{\epsilon_w^{(i)} = \frac{i-1}{K-1}\}_{i=1}^K$ for phase field regularization, as illustrated in

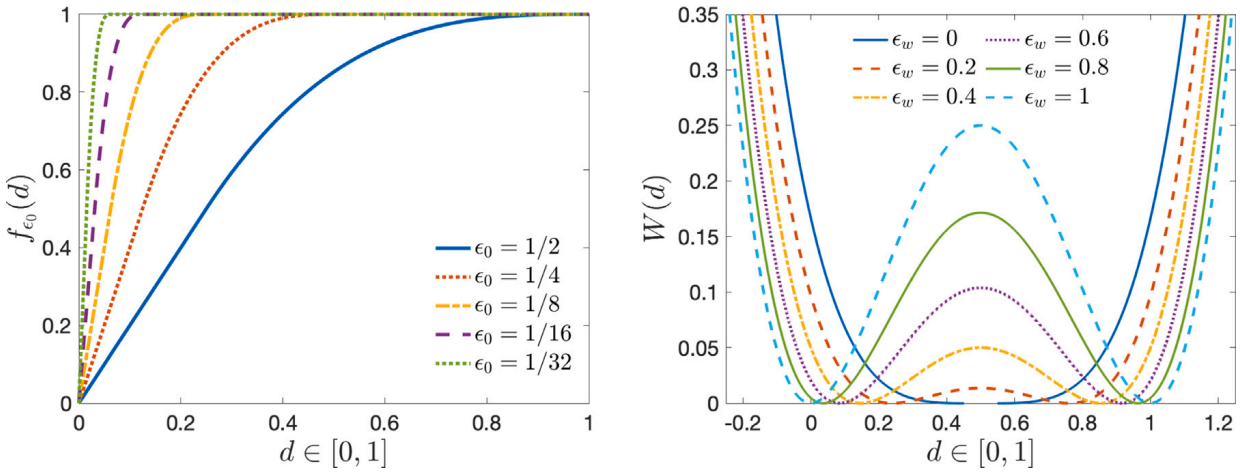

Fig. 1. Plots of sparsity-enforcing functions versus design parameter d: (a) $f_{\epsilon_0}(d)$ in (27) to approximate the ℓ_0-norm, controlled by ϵ_0; (b) the proposed double well function $W(d)$ in (29), evolving from a single well at $\epsilon_w = 0$ to a double well at $\epsilon_w = 1$.

Fig. 1. Each ith continuation iteration employs the previous optimal solution $d_{\text{opt}}^{(i-1)}$ as an initial guess. These continuation processes terminate when the specified stopping criteria are met. For ℓ_0-norm regularization (27), the hyperparameter value ϵ_0 directly controls the interface thickness. Hence, the continuation scheme stops when the interface thickness reaches a user-defined tolerance, such as the multi-material additive manufacturing precision. Regarding phase field regularization (29), the continuation process stops when a full double well forms at $\epsilon_w = 1$. The number of intermediate steps in the continuation process is problem-dependent and selected as a trade-off between convergence and computational cost.

5. Gradient-based optimization

To solve the optimization problem (6), we employ the limited-memory Broyden–Fletcher–Goldfarb–Shanno (L-BFGS) optimization algorithm with box constraints on the design parameter $d \in [0,1]$. L-BFGS is widely recognized as one of the most efficient methods among Quasi-Newton optimization algorithms [79]. Instead of computing and storing a dense n-by-n Hessian matrix (or its inverse), where n is the dimension of the design parameters stemming from discretization, L-BFGS stores only a few vectors representing the previous designs and their corresponding gradients. These vectors contain local curvature information and enable the construction of a limited memory Hessian matrix, irrespective of the parameter dimensions.

5.1. Gradient of cost function with respect to the design parameter

We use the Lagrangian formalism to derive the gradient of the quadratically approximated cost function $\mathcal{J}_{\text{quad}}(d)$ with respect to the design parameter, denoted as d-gradient, to provide gradient information to l-BFGS-b. By substituting the trace estimators (25) into (16), we have

$$\mathcal{J}_{\text{quad}}(d) = \left(\bar{Q} + \frac{1}{2}\sum_{j\geq 1}^{N_{\text{eig}}} \lambda_j\right) + \beta_V \left(\left\langle \bar{Q}^m, C\,\bar{Q}^m \right\rangle + \frac{1}{2}\sum_{j\geq 1}^{N_{\text{eig}}} \lambda_j^2\right) + \beta_R\, R(d). \tag{31}$$

To evaluate the d-gradient, we consider a quadratic meta-Lagrangian functional

$$\begin{aligned}
&\mathcal{L}_{\text{quad}}(\mathbf{u},\mathbf{v},\{\lambda_j\},\{\psi_j\},\{\hat{\mathbf{u}}_j\},\{\hat{\mathbf{v}}_j\},\mathbf{u}^*,\mathbf{v}^*,\{\lambda_j^*\},\{\psi_j^*\},\{\hat{\mathbf{u}}_j^*\},\{\hat{\mathbf{v}}_j^*\},d)\\
&\quad = J_{\text{quad}}(d) + \langle \mathbf{v}^*, \partial_{\mathbf{v}}\bar{r}\rangle + \langle \mathbf{u}^*, \partial_{\mathbf{u}}\bar{r} + \partial_{\mathbf{u}}\bar{Q}\rangle\\
&\quad + \sum_{j=1}^{N_{\text{eig}}} \langle \psi_j^*, (\bar{Q}^{mm} - \lambda_j C^{-1})\psi_j\rangle\\
&\quad + \sum_{j=1}^{N_{\text{eig}}} \lambda_j^*(\langle \psi_j, C^{-1}\psi_j\rangle - 1) + \sum_{j=1}^{N_{\text{eig}}} \langle \hat{\mathbf{v}}_j^*, \partial_{\mathbf{vu}}\bar{r}\,\hat{\mathbf{u}}_j + \partial_{\mathbf{v}m}\bar{r}\,\psi_j\rangle\\
&\quad + \sum_{j=1}^{N_{\text{eig}}} \langle \hat{\mathbf{u}}_j^*, \partial_{\mathbf{uv}}\bar{r}\,\hat{\mathbf{v}}_j + \partial_{\mathbf{uu}}\bar{r}\,\hat{\mathbf{u}}_j + \partial_{\mathbf{uu}}\bar{Q}\,\hat{\mathbf{u}}_j + \partial_{\mathbf{u}m}\bar{r}\,\psi_j + \partial_{\mathbf{u}m}\bar{Q}\,\psi_j\rangle
\end{aligned} \tag{32}$$

where $(\cdot^*)$ denotes the adjoint variables, $(\hat{\cdot})$ denotes the incremental variables, and $\{\cdot\}$ is the abbreviation of $\{\cdot\}_{n=1}^{N_{\text{eig}}}$. The terms on the right hand side of (32), respectively, are: the quadratically approximated cost function (31), the state problem (18), the adjoint

problem (19), the generalized eigenvalue problems (26), the orthonormality constraint of the eigenvectors, the incremental state problem (22) for the directions of the eigenvectors, and the incremental adjoint problem (23) for the directions of the eigenvectors. To compute the design gradient, we need to calculate five sets of functional derivatives to solve for the corresponding five sets of adjoint variables $(\mathbf{u}^*, \mathbf{v}^*, \{\psi_j^*\}, \{\hat{\mathbf{u}}_j^*\}, \{\hat{\mathbf{v}}_j^*\})$ in (32), while the adjoint variable set for the eigenvalue set $\{\lambda_j^*\}$ is not required due to its independency of the design parameter d.

By vanishing the first variation of (32) with respect to the eigenvalue set $\{\lambda_j\}$, the only contributing terms are the quadratically approximated cost function and the orthonormality constraint of the eigenvectors, such that

$$\{\psi_j^*\} = \left(\frac{1}{2} + \beta_V\, \lambda_j\right) \{\psi_j\}, \quad j = 1, \dots, N_{\text{eig}}. \tag{33}$$

Upon equating the first variations of (32) to zero with respect to $\mathbf{v}_j$ and $\mathbf{u}_j$ lead to the incremental state problem: *Find* $\hat{\mathbf{u}} \in \mathcal{U}$*, such that*

$$\left\langle \tilde{\mathbf{v}}, \partial_{\mathbf{vu}} \bar{r}\, \mathbf{u}_j^* \right\rangle = -\left\langle \tilde{\mathbf{v}}, \partial_{\mathbf{v}m} \bar{r}\, \psi_j^* \right\rangle, \quad \forall \tilde{\mathbf{v}} \in \mathcal{V}, \tag{34}$$

and the incremental adjoint problem: *Find* $\hat{\mathbf{v}} \in \mathcal{V}$*, such that*

$$\left\langle \tilde{\mathbf{u}}, \partial_{\mathbf{uv}} \bar{r}\, \mathbf{v}_j^* \right\rangle = -\left\langle \tilde{\mathbf{u}}, \partial_{\mathbf{uu}} \bar{r}\, \hat{\mathbf{u}}_j^* + \partial_{\mathbf{uu}} \bar{Q}\, \hat{\mathbf{u}}_j^* + \partial_{\mathbf{u}m} \bar{r}\, \psi_j^* + \partial_{\mathbf{u}m} \bar{Q}\, \psi_j^* \right\rangle, \ \forall \tilde{\mathbf{u}} \in \mathcal{U}, \tag{35}$$

similar to (22) and (23), respectively. In combination with (33), we can formulate the adjoint variables for the incremental state and adjoint problems individually for each eigenvector as

$$\{\hat{\mathbf{u}}_j^*\} = \left(\frac{1}{2} + \beta_V\, \lambda_j\right) \{\hat{\mathbf{u}}_j\}, \quad j = 1, \dots, N_{\text{eig}}, \tag{36}$$

$$\{\hat{\mathbf{v}}_j^*\} = \left(\frac{1}{2} + \beta_V\, \lambda_j\right) \{\hat{\mathbf{v}}_j\}, \quad j = 1, \dots, N_{\text{eig}}. \tag{37}$$

By vanishing the first variation of the Lagrangian functional (32) with respect to the adjoint and the state, we obtain the linear state problem: *Find* $\mathbf{u}^* \in \mathcal{U}$*, such that*

$$\begin{aligned} \langle \tilde{\mathbf{v}}, \partial_{\mathbf{vu}} \bar{r}\, \mathbf{u}^* \rangle = &- 2\beta_V \langle \tilde{\mathbf{v}}, \partial_{\mathbf{v}m} \bar{r}\, (C \partial_m \bar{r}) \rangle - \sum_{j=1}^{N_{\text{eig}}} \langle \tilde{\mathbf{v}}, \partial_{\mathbf{v}mu} \bar{r}\, \hat{\mathbf{u}}_j\, \psi_j^* + \partial_{\mathbf{v}mm} \bar{r}\, \psi_j\, \psi_j^* \rangle \\ &- \sum_{j=1}^{N_{\text{eig}}} \langle \tilde{\mathbf{v}}, \partial_{\mathbf{vuu}} \bar{r}\, \hat{\mathbf{u}}_j\, \hat{\mathbf{u}}_j^* + \partial_{\mathbf{vu}m} \bar{r}\, \psi_j\, \hat{\mathbf{u}}_j^* \rangle, \quad \forall \tilde{\mathbf{v}} \in \mathcal{V}, \end{aligned} \tag{38}$$

and linear adjoint problem: *Find* $\mathbf{v}^* \in \mathcal{V}$*, such that*

$$\begin{aligned} \langle \tilde{\mathbf{u}}, \partial_{\mathbf{uv}} \bar{r}\, \mathbf{v}^* \rangle = &- \langle \tilde{\mathbf{u}}, \partial_{\mathbf{u}} \bar{Q} \rangle - 2\beta_V \langle \tilde{\mathbf{u}}, \partial_{\mathbf{u}m} \bar{r}\, (C \partial_m \bar{r}) \rangle - \langle \tilde{\mathbf{u}}, \partial_{\mathbf{uu}} \bar{r}\, \mathbf{u}^* + \partial_{\mathbf{uu}} \bar{Q}\, \mathbf{u}^* \rangle \\ &- \sum_{j=1}^{N_{\text{eig}}} \langle \tilde{\mathbf{u}}, \partial_{\mathbf{u}m\mathbf{v}} \bar{r}\, \hat{\mathbf{v}}_j\, \psi_j^* + \partial_{\mathbf{u}m\mathbf{u}} \bar{r}\, \hat{\mathbf{u}}_j\, \psi_j^* + \partial_{\mathbf{u}mm} \bar{r}\, \psi_j\, \psi_j^* \rangle \\ &- \sum_{j=1}^{N_{\text{eig}}} \langle \tilde{\mathbf{u}}, \partial_{\mathbf{uvu}} \bar{r}\, \hat{\mathbf{u}}_j\, \hat{\mathbf{v}}_j^* + \partial_{\mathbf{uv}m} \bar{r}\, \psi_j\, \hat{\mathbf{v}}_j^* \rangle \\ &- \sum_{j=1}^{N_{\text{eig}}} \langle \tilde{\mathbf{u}}, \partial_{\mathbf{uuv}} \bar{r}\, \hat{\mathbf{v}}_j\, \hat{\mathbf{u}}_j^* + \partial_{\mathbf{uuu}} \bar{r}\, \hat{\mathbf{u}}_j\, \hat{\mathbf{u}}_j^* + \partial_{\mathbf{uuu}} \bar{Q}\, \hat{\mathbf{u}}_j\, \hat{\mathbf{u}}_j^* + \partial_{\mathbf{uuu}m} \bar{r}\, \psi_j\, \hat{\mathbf{u}}_j^* \rangle, \\ &\forall \tilde{\mathbf{u}} \in \mathcal{U}. \end{aligned} \tag{39}$$

And finally, having all the adjoint variables, the d-gradient is obtained by

$$\langle \tilde{d}, D_d J_{\text{quad}}(d) \rangle = \langle \tilde{d}, \partial_d \mathcal{L}_{\text{quad}} \rangle. \tag{40}$$

The procedures for computing the quadratically approximated cost function and its gradient with respect to the design parameter are summarized in Algorithm 2. In summary, the computational cost incurred for the evaluation of $\mathcal{J}_{\text{quad}}(d)$ in (31) consists of one state problem, one linear adjoint problem and $4(N_{\text{eig}} + N_o)$ linear PDEs resulting from the double-pass randomized algorithm in Algorithm 1, and the computation of the d-gradient requires the solution of $2(N_{\text{eig}} + 1)$ linear PDEs.

6. Problem formulation: Optimal design of insulation components

In this section, we implement the described design under uncertainty framework to the specific context of designing silica aerogel insulation components, retaining both mechanical stability and insulation performance. This entails presenting the thermomechanical PDE model for porous materials, defining the design objectives, representing uncertain design parameters, and formulating the multi-objective optimal design problem.

Algorithm 2: Evaluation of the $\mathcal{J}_{\text{quad}}$ and its d-gradient

Input : Design objective (5) and weak form of the PDF (2).
Output: Approximated cost function $\mathcal{J}_{\text{quad}}(d)$ and its gradient with respect to the design parameter d.

1 Solve for m-gradient (20)
2 Solve for m-Hessian (24)
3 Solve for generalized eigenpairs with Algorithm 1
4 Compute $\mathcal{J}_{\text{quad}}$ by (31)
5 Solve the linear state problem (38)
6 Solve the linear adjoint problem (39)
7 Obtain the d-gradient (40)

6.1. Forward thermomechanical model

We employ a thermomechanical model of silica aerogel materials built upon a continuum mixture theory [56]. The model considers incompressible solid aerogel network and compressible fluid (gaseous) phases within the materials. According to the mixture theory, each phase independently follows its own motion, balance laws, internal energy, and entropy while adhering to the overall balance laws of the entire mixture. Consequently, a set of four PDEs is derived that governs the heat transfer in the solid and fluid phases, the deformation in the solid phase and the evolution of pore pressure. In the context of designing insulation components, we specifically consider steady-state and static conditions, which simplify the governing equations. The strong form of the PDEs corresponding to (1) is expressed as,

$$\begin{cases} -\nabla\cdot(\phi_s\,\kappa_s\,\nabla\theta_s)+h(\theta_s-\theta_f)=0 & \text{in} \quad \Omega,\\ -\nabla\cdot(\phi_f\,\kappa_f\,\nabla\theta_f)-h(\theta_s-\theta_f)=0 & \text{in} \quad \Omega,\\ \theta_s=\theta_f=\theta^{\dagger} & \text{on} \quad \Gamma_d,\\ -\phi_s\,\kappa_s\,\nabla\theta_s=h_{\text{air}}(\theta_s-\theta_{\text{amb}}) & \text{on} \quad \Gamma_c,\\ -\phi_f\,\kappa_f\,\nabla\theta_f=h_{\text{air}}(\theta_f-\theta_{\text{amb}}) & \text{on} \quad \Gamma_c, \end{cases} \tag{41}$$

$$\begin{cases} C\,p+(\nabla\cdot\mathbf{u}_s)=0 & \text{in} \quad \Omega,\\ -\nabla\cdot\mathbf{T}_s'-(2\,\phi_f-1)\,\nabla p=0 & \text{in} \quad \Omega,\\ \mathbf{u}_s=\mathbf{u}_s^{\dagger} & \text{on} \quad \Gamma_e,\\ \mathbf{n}\mathbf{T}_s'=\mathbf{t} & \text{on} \quad \Gamma_t. \end{cases} \tag{42}$$

In the above equations, $\Omega\subset\mathbb{R}^d$ is an open and bounded domain with Lipschitz boundary $\partial\Omega$, and $\Gamma_d,\Gamma_e\subset\partial\Omega$ denote the Dirichlet portions and $\Gamma_c,\Gamma_t\subset\partial\Omega$ indicate the Neumann portions of $\partial\Omega$ such that $\Gamma_d\cup\Gamma_c=\partial\Omega$, $\Gamma_d\cap\Gamma_c=\emptyset$, $\Gamma_e\cup\Gamma_t=\partial\Omega$, and $\Gamma_e\cap\Gamma_t=\emptyset$. The state variables θ_s, θ_f, $\mathbf{u}_s$, and p represent the solid and fluid temperatures, solid displacement, and fluid pressure, respectively, defined over the domain Ω. The conductivity associated with the solid and fluid phases is denoted as κ_s and κ_f, h represents the inter-constituent convection coefficient, and C represents the fluid compressibility. The temperature and solid displacement are subject to fixed values $\theta^{\dagger}$ and $\mathbf{u}_s^{\dagger}$ at the boundaries Γ_d and Γ_e, respectively. At Γ_c, we consider convective heat transfer with a coefficient h_{air} and ambient temperature θ_{amb} and at the boundary Γ_t with unit outward vector $\mathbf{n}$, a traction vector $\mathbf{t}$ is imposed. For a visual representation of the thermal and mechanical boundary conditions considered in the numerical examples, please refer to Figs. 12 and 3. The design problem involves the determination of spatial distributions of the fluid volume fraction (porosity), denoted by $\phi_f(\mathbf{x})$, which is equivalently expressed as $1-\phi_s(\mathbf{x})$ with $\phi_s(\mathbf{x})$ being the solid volume fraction. In (42), the effective solid stress is

$$\mathbf{T}_s'=2\,\mu\,\mathbf{E}_s+\lambda\,\text{tr}(\mathbf{E}_s)\,\mathbf{I}\quad\text{with}\quad\mathbf{E}_s=\frac{1}{2}\big(\nabla\mathbf{u}_s+(\nabla\mathbf{u}_s)^T\big), \tag{43}$$

where $\mathbf{E}_s$ is the solid strain and λ and μ are the Lamé constants. Determining the model parameters κ_s, κ_f, h, K, C, and μ from experimental data of silica aerogel is demonstrated in [56] and assumed to be known here.

The weak formulation of the PDEs (41) and (42), corresponding to (2), can be expressed as follows: *Find* $\mathbf{u}=(\theta_s,\theta_f,\mathbf{u}_s,p)\in\mathcal{U}$, *such that*

$$\begin{aligned} -\big\langle\phi_s\kappa_s\nabla\theta_s,\nabla z_s\big\rangle-\big\langle h(\theta_s-\theta_f),z_s\big\rangle-\big\langle\phi_s h_{\text{air}}(\theta_s-\theta_{\text{amb}}),z_s\big\rangle &= 0,\\ -\big\langle\phi_f\kappa_f\nabla\theta_f,\nabla z_f\big\rangle+\big\langle h(\theta_s-\theta_f),z_f\big\rangle-\big\langle\phi_f h_{\text{air}}(\theta_f-\theta_{\text{amb}}),z_f\big\rangle &= 0,\\ -\Big\langle(\lambda+\frac{1-2\phi_f}{C})(\nabla\cdot\mathbf{u}_s)\mathbf{I}+\mu\big(\nabla\mathbf{u}_s+(\nabla\mathbf{u}_s)^T\big),\boldsymbol{w}_u\Big\rangle+\big\langle\mathbf{t},\boldsymbol{w}_u\big\rangle &= 0, \end{aligned} \tag{44}$$

for all choices of adjoint variables $\mathbf{v}=(z_s,z_f,\boldsymbol{w}_u)\in\mathcal{V}$, where $\mathcal{U}$ and $\mathcal{V}$ are Hilbert spaces. We define Q_T and Q_M as measures of thermal insulation and mechanical stability, respectively, for the insulation component over domain Ω,

$$Q_T=\frac{1}{2}\sum_{i=s,f}\big\langle\phi_i\,\kappa_i\,\nabla\theta_i,\nabla\theta_i\big\rangle+\sum_{i=s,f}\big\langle\phi_i h_{\text{air}}(\theta_i-\theta_{\text{amb}}),\theta_i\big\rangle,$$

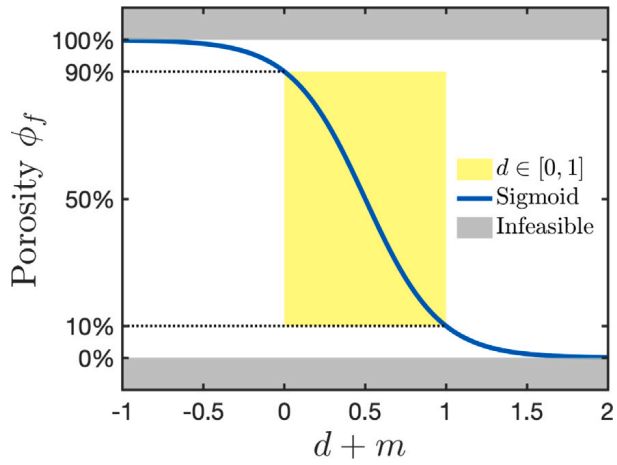

Fig. 2. The sigmoid function asymptotically bounding porosity in physically meaningful range $\phi_f \in [0\%, 100\%]$. The x-axis represents $d+m$, where the $d \in [0,1]$ is the design parameter and $m \sim \mathcal{N}(0, C)$ is the uncertain parameter.

$$Q_M = \frac{1}{2}\langle \mathbf{T}'_s, \mathbf{E}_s \rangle + \langle \mathbf{t}, \mathbf{u}_s \rangle. \tag{45}$$

6.2. Uncertain design parameter

Owing to imprecise control of silica aerogel properties, substantial uncertainty is associated with the porosity value within the insulation component. This uncertainty is spatially correlated and exhibits anisotropic properties, arising from the layer-by-layer deposition of aerogel ink during the additive manufacturing process [11]. To effectively model the variability in porosity, we represent material porosity $\phi_f(\mathbf{x})$ within the range of $[0\%, 100\%]$ using a density-like design parameter $d(\mathbf{x})$ in the range $[0,1]$, complemented by the uncertain parameter $m(\mathbf{x})$ introduced in Section 2.2, as

$$\phi_f(\mathbf{x}) = f\left(d(\mathbf{x}) + m(\mathbf{x})\right). \tag{46}$$

As illustrated in Fig. 2, $f(\cdot)$ is a sigmoid function that remains almost linear within $\phi_f \in [10\%, 90\%]$ and $d+m \in [0,1]$ to mitigate the influence on the correlation length L_c while ensuring porosity values asymptotically stay within the physically valid range of $\phi_f \in [0\%, 100\%]$. In other words, the mapping described in (46) is employed primarily to constrain variations in porosity caused by the uncertain parameter.

Another essential requirement for the design of insulation components is achieving spatial sparsity in the porosity distribution. Ideally, this involves components with two distinct aerogel inks with different porosities and a precisely controlled interface thickness. Such a design minimizes the number of nozzles required and reduces the fabrication time within the additive manufacturing process. To address this solution sparsity, the proposed regularization terms discussed in Section 4 are incorporated into the optimization process.

6.3. Multi-objective PDE-constrained optimal design under uncertainty

The optimal design problem described in Section 2.3 can be extended to accommodate multiple, potentially conflicting objectives $\{Q_p\}_{p=1}^P$, each of which holds varying degrees of importance in the overall design process. In this context, the cost functional for the resulting multi-objective optimal design is expressed as follows:

$$\mathcal{J}(d) = \sum_{p=1}^{P} \left(\beta_{E_p} \mathbb{E}[Q_p(d,m)] + \beta_{V_p} \mathbb{V}[Q_p(d,m)] \right) + \beta_R R(d), \tag{47}$$

where the weights $\{\beta_{V_p}\}_{p=1}^P$ and β_R govern the proportionate significance of the variance of the design objectives and the regularization term relative to the means of design objectives, characterized by β_{E_p}. In the numerical experiments detailed in Section 7, we consider the multi-objective design of components to enhance both their mechanical strength and thermal insulation properties. To achieve this, we define the total design objective Q as a weighted sum of the thermal and mechanical objectives outlined in (45), given by

$$Q = \beta_M Q_M - Q_T, \tag{48}$$

where β_M represents the mechanical weight that governs the trade-off between thermal insulation and mechanical stability. Subsequently, without loss of generality, we specialize (47) by $P = 2$, $\beta_{E_1} = \beta_M$, $\beta_{E_2} = -1$, $\beta_{V_1} = \beta_V \beta_M$, and $\beta_{V_2} = -\beta_V$. As a result, the mean–variance cost function and the risk-averse PDE-constrained optimal design under uncertainty take the forms presented in (5) and (6), respectively.

6.4. Hyper-parameters

The proposed design under uncertainty framework involves various hyper-parameters that significantly impact the resulting optimal solutions. These hyper-parameters encompass the variance, correlation length, and anisotropy of the Gaussian random field in (3), the weight factors introduced within the cost functional (5), and the parameters associated with the regularization term in (27) and (29). The coefficients of the Gaussian random field are intricately linked with material properties and can be determined, in conjunction with the model parameters, from experimental measurements. Optimization techniques like the one implemented in [63] provide suitable means for such inference. Identifying the Pareto design set via multi-objective optimization, e.g., [80] provides insights into the optimal trade-offs between conflicting thermal and mechanical objectives and their variances, aiding in decision-making and objective prioritization for the final design. A practical method for selecting the Tikhonov regularization weight β_{tik} is the L-curve method [81], which strikes a balance between stabilizing the design parameter and minimizing the design objective's mean and variance. Alternatively, Morozov's discrepancy principle, involving a meta-optimization problem [82–84] can be leveraged. The parameter β_{well} in phase field regularization controls the interface thickness between sparse design parameters and is selected to balance spatial gradient and the double-well functions.

7. Numerical examples

This section presents numerical experiments utilizing the proposed design under uncertainty framework for two aerogel insulation scenarios in which the design parameter is the discretization of a random field. The objective is to achieve both thermal insulation and mechanical stability while mitigating uncertainty in the design process, as formulated in (48), (5), and (6). The first example involves an L-shape component, which demonstrates key aspects of the framework. These include assessing the accuracy and cost of the quadratic approximation of cost functional, analyzing the effects of mechanical and variance weights on the optimal design, and evaluating the scalability of the optimization under uncertainty algorithm concerning the dimension of the design parameters. The second example is the design of thermal breaks within an envelope-column system that demonstrates the continuation schemes for both ℓ_0 and phase-field regularizations.

In both examples, the parameter values for the multiphase model in (41) and (42) are $\kappa_s = 0.477$, $\kappa_f = 0.085$, $h = 81059$, $C = 0.25$, $\lambda = 6.77$, and $\mu = 3.38$, adopted from [56]. For all the numerical experiments, unless explicitly specified, we utilize the quadratic approximation of the design objective with $N_{\text{eig}} = 25$ dominant eigenvalues and the oversampling factor as $N_o = 20$. The uncertain parameter m is the Gaussian random field with Matérn covariance, with mean $\bar{m} = 0$, the variance of $\sigma^2 = 0.5^2$, correlation lengths of $L_c = 0.5$. To emphasize dominant anisotropy along the x-direction, we set $\vartheta_x = 1$ and $\alpha = 90°$, while assigning a small value to $\vartheta_y = 1\times10^{-4}$ to ensure numerical stability. The computational implementation of the proposed design under uncertainty framework relies on a series of open-source libraries, including, FeniCS[1] [85] for finite element solution of the forward model, hIPPYLib[2] [86–88] for the Gaussian random field in (3) and the trace estimator in Algorithm 1, SOUPy[3] [31,36] for quadratic approximation of the design objective described in Section 3, and l-BFGS-b optimizer in Scipy[4] [89].

7.1. L-shape insulation component

The domain of the L-shaped insulation component is illustrated in Fig. 3 . For the heat transfer model in (41), the Neumann boundary conditions are taken into account, entailing $\theta_{\text{amb}} = 1$ at the outer boundary Γ_1, $\theta_{\text{amb}} = 0$ at the inner boundary Γ_2, and insulated condition ($h_{\text{air}} = 0$) on Γ_3. The boundary conditions of the mechanical model in (42), consists of prescribing uniform traction load $\|\mathbf{t}\| = 1$ along and opposite direction of the unit vectors on Γ_1, fixed solid displacement $\mathbf{u}_s = 0$ on Γ_2, and setting the displacement component along the unit vectors to zero on Γ_3. Unless specified otherwise, a finite element mesh with 8587 nodes (design parameter dimension) is employed.

Fig. 4 demonstrates the influence of the uncertain parameter m, originating from an anisotropic Gaussian random field in (3), on the porosity field $\phi_f(\mathbf{x})$. An illustrative example of porosity design is shown in this figure, along with two sets of porosity samples, evaluated from the samples of uncertain parameter m and (46). The higher correlation length of m yields a distinct anisotropic of the material porosity in Fig. 4(e - g). Such anisotropy can effectively model horizontal layer-by-layer manufacturing of the component, capturing the correlation of aerogel ink properties within individual layers as well as the distinct properties among various layers.

To evaluate the effectiveness of the Robin condition in minimizing the boundary effect on the Gaussian random field with Matérn covariance in (3), we computed the diagonal entries of the discretized covariance operator $\mathcal{C}$. Fig. 5(a) shows the exact marginal variance of the anisotropic uncertain parameter m (see [59] for a more efficient marginal variance estimator). The deviation of the marginal variance from a constant field (the blue area along the horizontal boundaries covering roughly 6% of the domain) in this figure indicates a relatively small undesired boundary effect, which is significantly mitigated by the imposed Robin boundary conditions with a constant coefficient as described in Section 2.2. The horizontal noise in this figure results from assigning a small value to $\vartheta_y = 1\times10^{-4}$ in the anisotropic tensor (4) for numerical stability. Furthermore, Fig. 5(b–c) shows the spatial correlation structures at three different locations within the domain, indicating minimal boundary effects in this problem based on the largely undistorted elliptical contours.

[1] https://fenicsproject.org
[2] https://github.com/hippylib/hippylib
[3] https://github.com/hippylib/soupy
[4] https://scipy.org

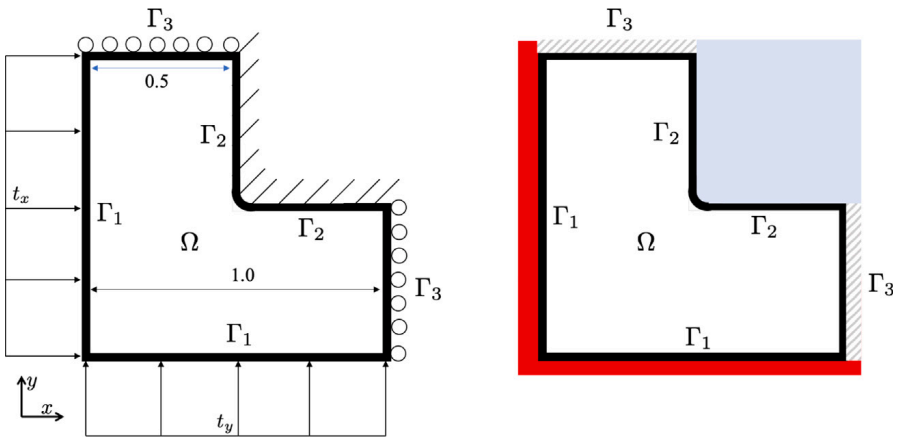

Fig. 3. Domain of the L-shape insulation component used for numerical experiments, illustrating both mechanical (left) and thermal boundary conditions (right). In the thermal boundary conditions, red and blue indicate ambient temperatures $\theta_{\text{amb}} = 1$ and $\theta_{\text{amb}} = 0$, respectively. (For interpretation of the references to color in this figure legend, the reader is referred to the web version of this article.)

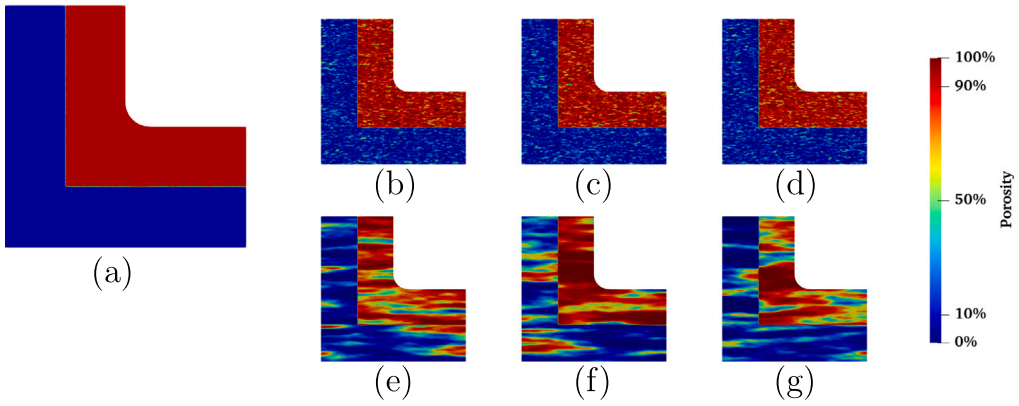

Fig. 4. Effect of uncertain parameter $m(\mathbf{x})$ on the aerogel porosity field. (a) Illustrative half-and-half porosity design example at the mean of uncertain parameter $\bar{m} = 0$. Samples of uncertain porosity field $\phi_f(\mathbf{x})$ using the map (46) and i.i.d. samples of m: (b–d) small correlation length $L_c = 0.02$ and (e–g) large correlation length $L_c = 0.5$.

To assess the accuracy and efficiency of the quadratic approximations on the optimal design solution, we conduct a comparison with the Monte Carlo method. Fig. 6 shows the Monte Carlo estimations of the mean (7) and variance (8) of the design objective for various numbers of samples N_{mc}, along with the corresponding quadratic approximations in (11) and (15) over different numbers of dominant eigenvalues N_{eig}. As expected, both estimations converge towards the same values as the number of samples and dominant eigenvalues increases. The relatively small variation in the mean values of the design objective for different numbers of samples, despite the high uncertainty in porosity (see Fig. 4), can be attributed to the domain size considered for this problem in relation to the parameter values.

Fig. 7 compares two scenarios characterized by different variances and correlation lengths of the uncertain parameter m and the mechanical weight β_M. It includes the optimal design $d_{\text{opt}}(\mathbf{x})$ and the probability distributions of the design objectives, including Q_T and Q_M as defined in (45), and Q as defined in (48). For each scenario, the solutions are obtained using the Monte Carlo estimation and the quadratic Taylor approximation of the mean and variance of the design objective, as well as the deterministic solution, where the uncertain parameter m is set to zero, resulting in a deterministic value for Q. The d-gradient used for optimization via the Monte Carlo method is adopted from [31], which involves N_{mc} state PDE and N_{mc} linearized PDE solutions. As expected, the optimal design morphologies are almost identical in the Monte Carlo, quadratic approximation, and deterministic cases for the scenario involving low variance and a large correlation length, as shown in Fig. 7(a–c). In contrast, distinct morphologies are obtained for the large uncertainty scenario (high variance and large correlation length), as depicted in Fig. 7(d–f). More specifically, when comparing the design objectives obtained through quadratic approximation and Monte Carlo methods (as shown in Fig. 7(d,e)), we obtain relative errors in means of 0.1%,0.4%, and 0.2% along with relative errors in variances of 6.1%,13.8%, and 8.5%, respectively for Q_T, Q_M. The relative errors suggest that, in this specific problem, utilizing the quadratic Taylor expansion for linearizing the objective moments provides reasonably accurate optimal design solutions, even with significant uncertainty in the porosity field. Furthermore, in the low-uncertainty scenario, the deterministic objectives fall within the probability distributions of Q_T, Q_M, and Q obtained from the Monte Carlo and quadratic approximation. However, in the high-uncertainty scenario, the deterministic design

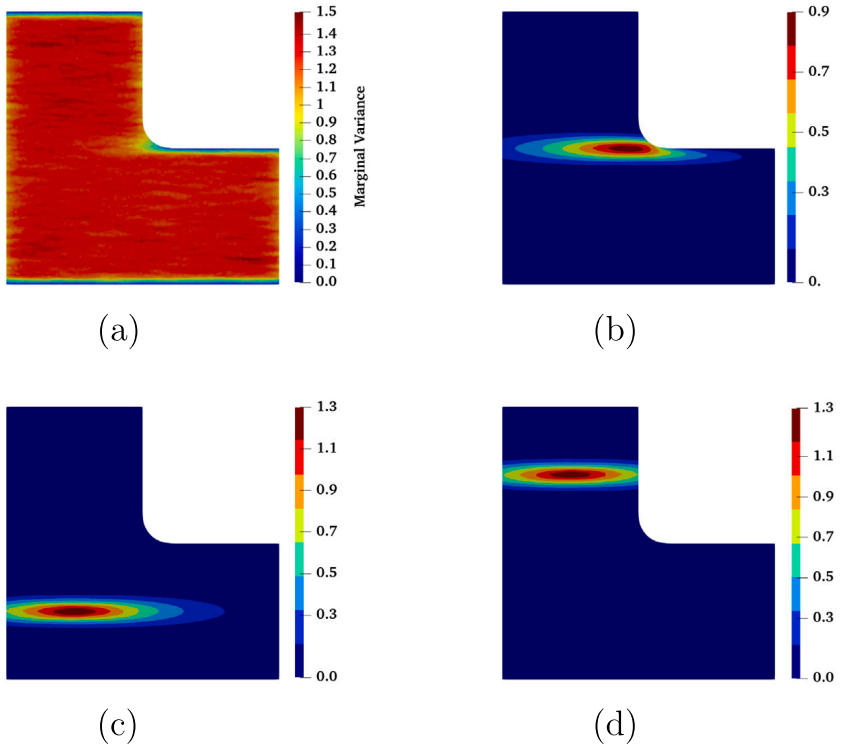

Fig. 5. Evaluating the effect of boundary on the Gaussian random field in (3): (a) marginal variance of the anisotropic uncertain parameter m with an estimated 6% of the domain area showing boundary effect, and point-wise correlation structure centered at (b) point (0.5, 0.5), (c) point (0.25, 0.25), (d) point (0.25, 0.75). Coordinates (x, y) are defined with respect to the bottom left corner of the L-shaped domain (refer to Fig. 3). The uncertain parameter m is characterized by a mean value of $\bar{m} = 0$, a variance of $\sigma^2 = 0.5^2$, correlation lengths of $L_c = 0.5$, anisotropy with $\vartheta_x = 1$, $\vartheta_y = 1 \times 10^{-4}$, and $\alpha = 90°$.

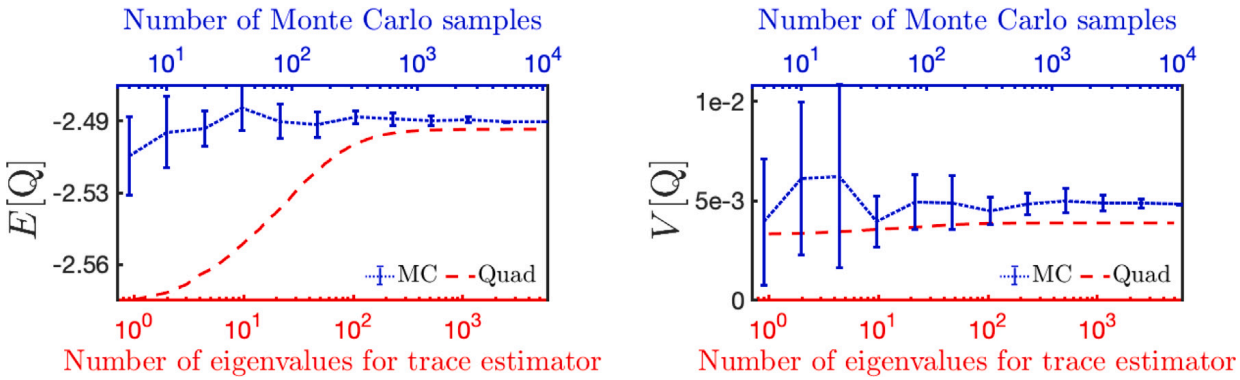

Fig. 6. Convergence plots of the estimated (left) mean and (right) variance of the design objective Q using the Monte Carlo estimations (denoted by *MC*) and the quadratic approximations (denoted by *Quad*). At each point, ten realizations of the uncertain parameter m are considered with variance $\sigma^2 = 0.5^2$ and correlation length $L_c = 0.5$.

objectives corresponding to Fig. 7(f) differ from the probability distributions associated with Fig. 7(d,e). This deviation reflects a trade-off, prioritizing uncertainty reduction over mean performance following the multi-objective formulation (5).

Next, we study the effect of the mechanical weight β_M in (48) and the variance weight β_V in (5) on the optimal design solutions via the quadratic approximation. Fig. 8 illustrates the outcomes of the optimal design problem for varied mechanical weight. The optimal design $d_{\text{opt}}(\mathbf{x})$ patterns shows that, as β_M increases, the low-porosity covers a larger portion of the domain and high-strength aerogel material (represented in red), leading to the emergence of mechanical supports aligned with the loading direction. Consistently, the trend of the trade-off between thermal insulation Q_T and mechanical strength Q_M are reflected in their probability distributions in Fig. 8 (d–f). Fig. 9 shows that as the variance weight β_V increases, the spatial patterns of the optimal designs $d_{\text{opt}}(\mathbf{x})$ begin to incorporate mechanical supports made of high-strength aerogel (represented in red) to augment mechanical strength of the component. Concurrently, regions of high-porosity aerogel (represented in blue) appear, enhancing the thermal insulation performance. These developing $d_{\text{opt}}(\mathbf{x})$ patterns lead to reduction of variance of both the thermal Q_T and mechanical Q_M

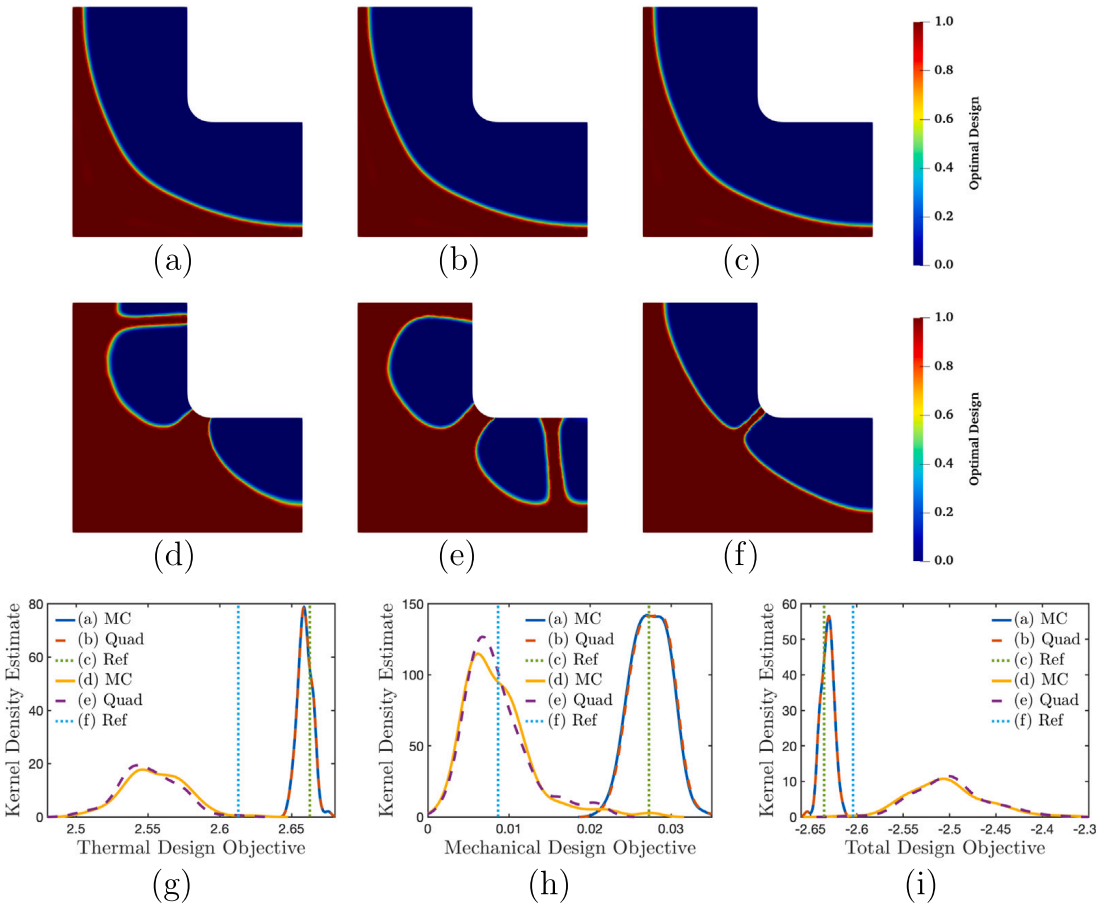

Fig. 7. Optimal design $d_{\text{opt}}(\mathbf{x})$ obtained using (a,d) Monte Carlo method (denoted by *MC*) with $N_{\text{mc}} = 150$ samples, (b,e) quadratic approximation (denoted by *Quad*) with $N_{\text{eig}} = 25$ dominant eigenvalues, (c,f) deterministic design in the absence of uncertainty $m = 0$ (denoted by *Ref*). Panels (a–c) correspond to $\sigma^2 = 0.1^2$, $L_c = 0.02$, $\beta_M = 1$, and $\beta_V = 1$, while panels (d–f) correspond to $\sigma^2 = 0.5^2$, $L_c = 0.02$, $\beta_M = 6$, and $\beta_V = 1$. The corresponding probability distributions of (g) thermal objective Q_T, (h) mechanical objective Q_M, and (i) total design objective Q.

objectives, as depicted in Fig. 9(d, e). Overall, increasing β_V reduces the design objective Q variance by trading off its mean values in Fig. 9(f).

Finally, we study the scalability of the PDE-constrained optimization under uncertainty algorithm with respect to the design dimension (number of nodes in the discretization of $d(\mathbf{x})$). This, in particular, depends on dimension-independent properties of two factors: (i) decay of the eigenvalues of the covariance-preconditioned Hessian computed using randomized trace estimator described in Section 3.2, and (ii) convergence rate of l-BFGS-b optimizer mentioned in Section 5. Fig. 10 displays the cost functional (5) and the norm of the gradient (40) against the number of l-BFGS-b iterations, as well as the decay of the absolute values of the generalized eigenvalues (26). These quantities are plotted for various dimensions of the design parameter, ranging from 5469 to 21,596, corresponding to the optimal design problem shown in Fig. 8(c). Using quadratic approximation, the objective functional exhibits fast decay, and the norm of the gradient falls below the tolerance of 1×10^{-4} within 100 iterations for all mesh resolutions. The negligible dependency of these plots on the mesh resolution implies that the gradient-based l-BFGS-b algorithm is independent of the number of uncertain parameters. Additionally, the eigenvalues display fast decay that is independent of the uncertain parameter dimension in Fig. 10(c), thus indicating that the randomized eigensolver for approximating the trace is also scalable with respect to the number of uncertain parameters. Fig. 11 shows the corresponding eigenfunction of the covariance-preconditioned Hessian of the design objective. The eigenvectors corresponding to larger eigenvalues inform the larger spatial scale of the design parameter, while the ones related to smaller eigenvalues are increasingly more oscillatory and less informative. Combining the two dimension-independent factors, one concludes that leveraging the quadratic Taylor approximation and stochastic optimization method results in scalable PDE-constrained optimal design under uncertainty with respect to the uncertain parameter dimension.

7.2. Design of thermal breaks in an envelope-column system

Fig. 12 illustrates the simulation domain of a building envelope-column system. The design domain of the aerogel thermal break is denoted by Ω, and Ω_c represents the non-design domain, a concrete column with high mechanical strength and high thermal conductivity. For the thermal model, the Neumann boundary conditions entail $\theta_{\text{amb}} = 1$ at the building exterior boundary Γ_1, $\theta_{\text{amb}} = 0$

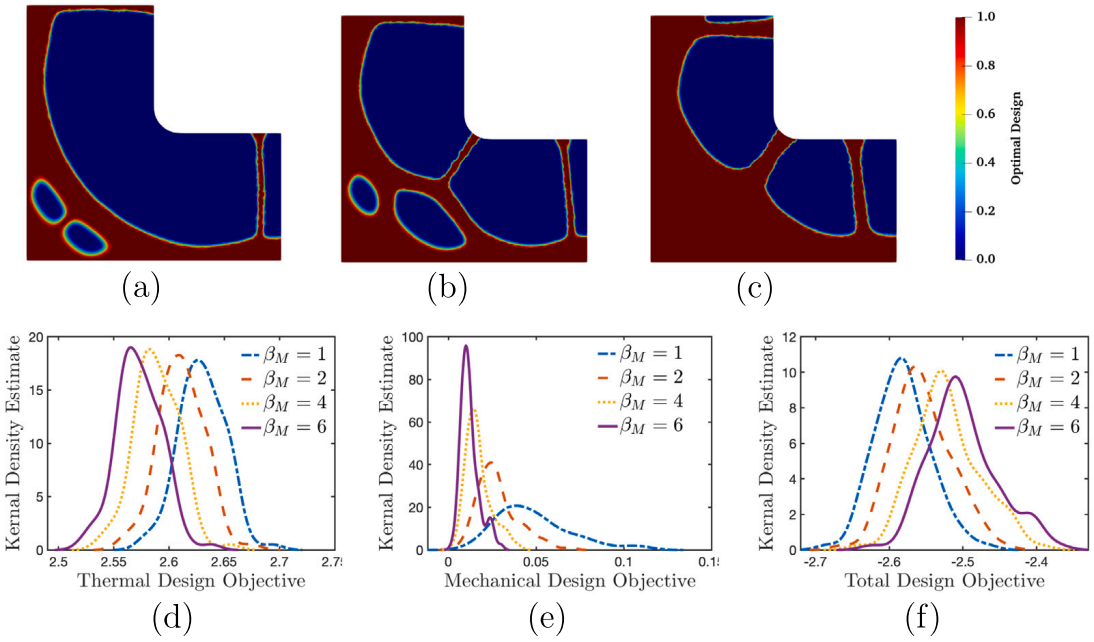

Fig. 8. Design under uncertainty results for different mechanical weights β_M. Optimal design $d_{\text{opt}}(\mathbf{x})$ for: (a) $\beta_M = 1$, (b) $\beta_M = 2$, and (c) $\beta_M = 6$. The corresponding probability distributions of (d) thermal objective Q_T, (e) mechanical objective Q_M, and (f) design objective Q. In all results, $\beta_V = 3$ and $\beta_R = 3 \times 10^{-5}$.

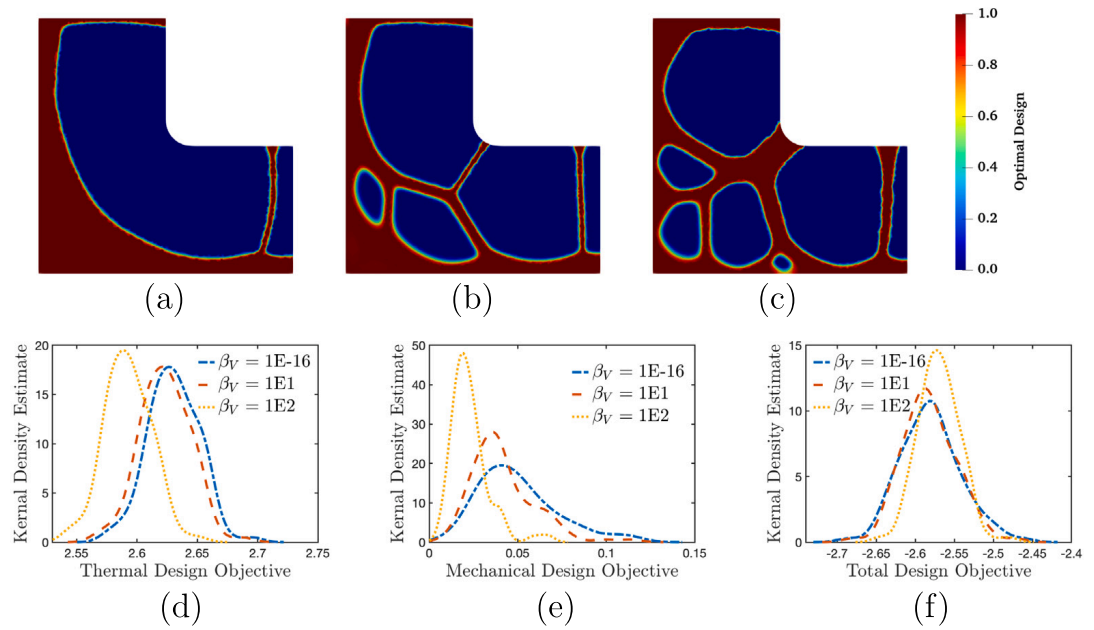

Fig. 9. Design under uncertainty results for different variance weights β_V. Optimal design $d_{\text{opt}}(\mathbf{x})$ for: (a) β_V = 1E-16, (b) β_V = 1E1, and (c) β_V = 1E2. The corresponding probability distributions of (d) thermal objective Q_T, (e) mechanical objective Q_M, and (f) design objective Q. In all results, $\beta_M = 1$ and $\beta_R = 4 \times 10^{-5}$.

at the interior boundary Γ_2, and insulated condition on Γ_3 are taken into account. The boundary conditions of the mechanical model in (42), consists of prescribing uniform traction load $\|\mathbf{t}\| = 1$ along and opposite direction of the unit vector on Γ_1, fixed displacement $\mathbf{u}_s = 0$ on Γ_2, and setting the displacement component along the unit vectors to zero on Γ_3. The thermomechanical behavior of the column over the domain Ω_c is modeled using linear elasticity with Young's modulus $E_c = 30$ and passion ratio $\nu_c = 0.3$ and heat transfer with thermal conductivity $\kappa_c = 5$. A finite element mesh with 7344 nodes is utilized to discretize the domain, resulting in a design parameter dimension of 6694 after excluding nodes within the column region. The mechanical and variance weights are also considered $\beta_M = 3$ and $\beta_V = 10$. Fig. 13 also illustrates the impact of two different samples of the uncertain parameter m on the porosity field $\phi_f(\mathbf{x})$ in a design example.

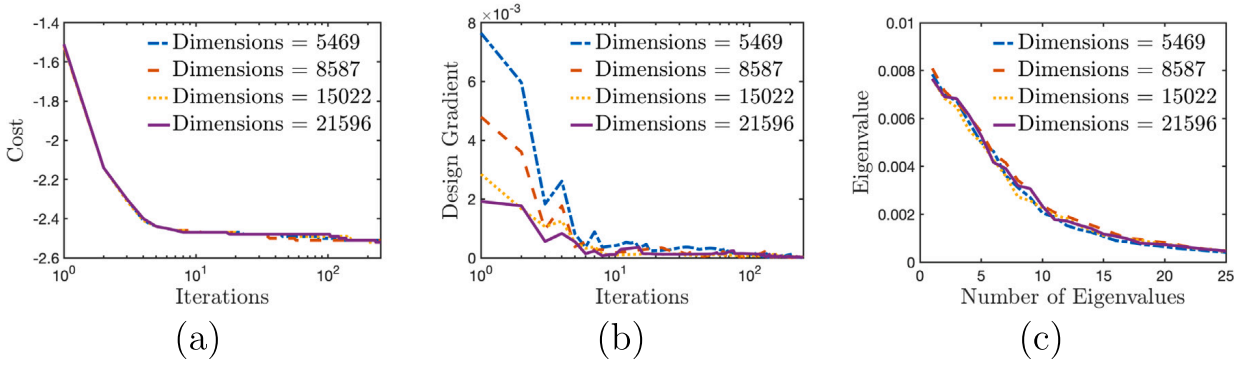

Fig. 10. The optimization solutions corresponding to Fig. 8(c) for different dimensions (discretization mesh) of the design parameter: (a) variation of the objective functional J_{quad} with the number of l-BFGS-b optimization steps, (b) variation of the norm of d-gradient with the number of l-BFGS-b optimization steps, (c) decay of the eigenvalues of the covariance-preconditioned Hessian. In all results, $\beta_M = 6$, $\beta_V = 3$, and $\beta_R = 3 \times 10^{-5}$.

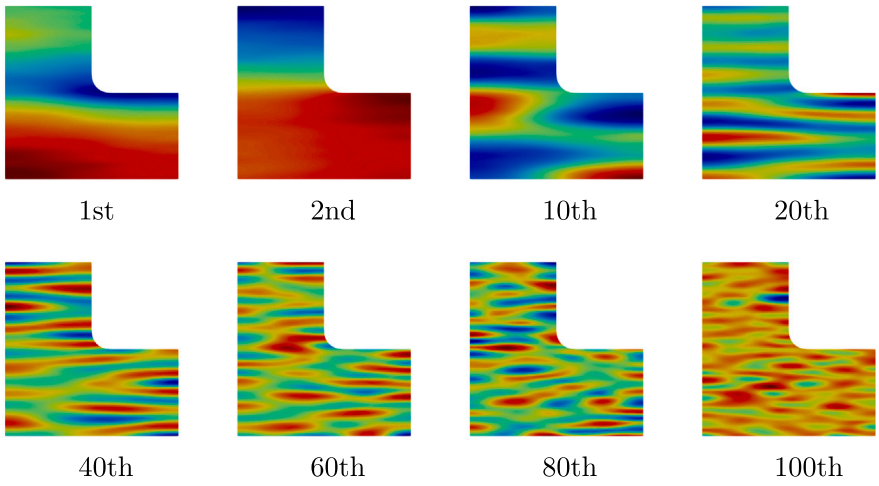

Fig. 11. Eigenfunctions of the covariance-preconditioned Hessian of the design objective corresponding to the eigenvalues decay shown in Fig. 10(c).

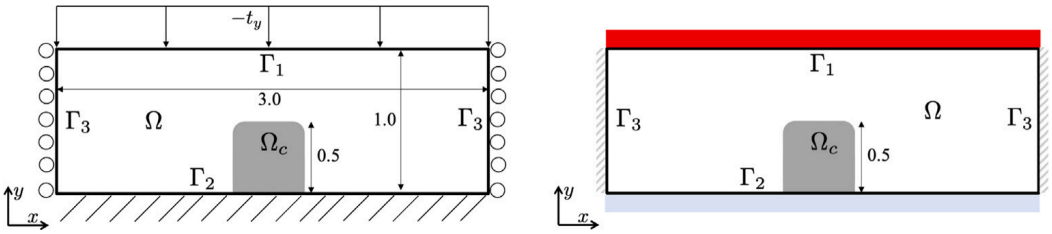

Fig. 12. The domain of a building envelope-column system used for numerical experiments, indicating both mechanical (left) and thermal (right) boundary conditions. The goal of the aerogel thermal break is to alleviate the heat flow between the building exterior and the concrete column with high thermal conductivity while remaining mechanically stable against the external environmental load imposed at Γ_1.

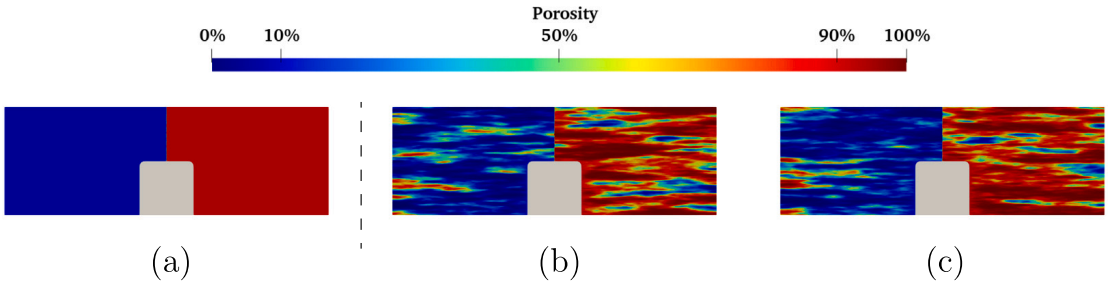

Fig. 13. Effect of uncertain parameter $m(\mathbf{x})$ on the aerogel porosity field for an illustrative porosity design example: (a) at the mean of the uncertain parameter $\bar{m} = 0$, (b) at two i.i.d. samples of m.

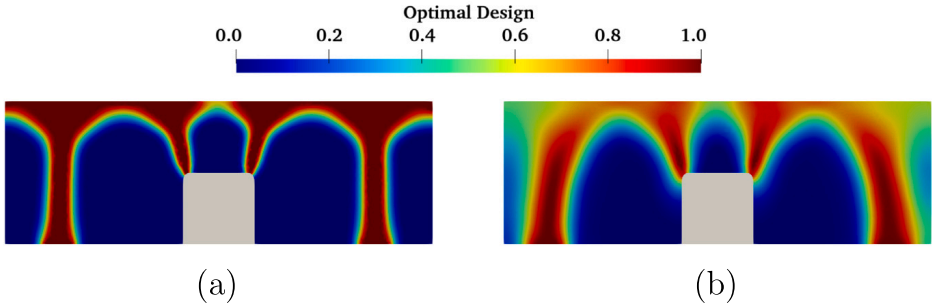

Fig. 14. Optimal design solutions $d^{\text{tik}}_{\text{opt}}(\mathbf{x})$ obtained using only Tikhonov regularization: (a) *Scenario I* with $\beta_{\text{tik}} = 1 \times 10^{-3}$ and a moderate interface thickness, (b) *Scenario II* with $\beta_{\text{tik}} = 4 \times 10^{-3}$ and a large interface thickness.

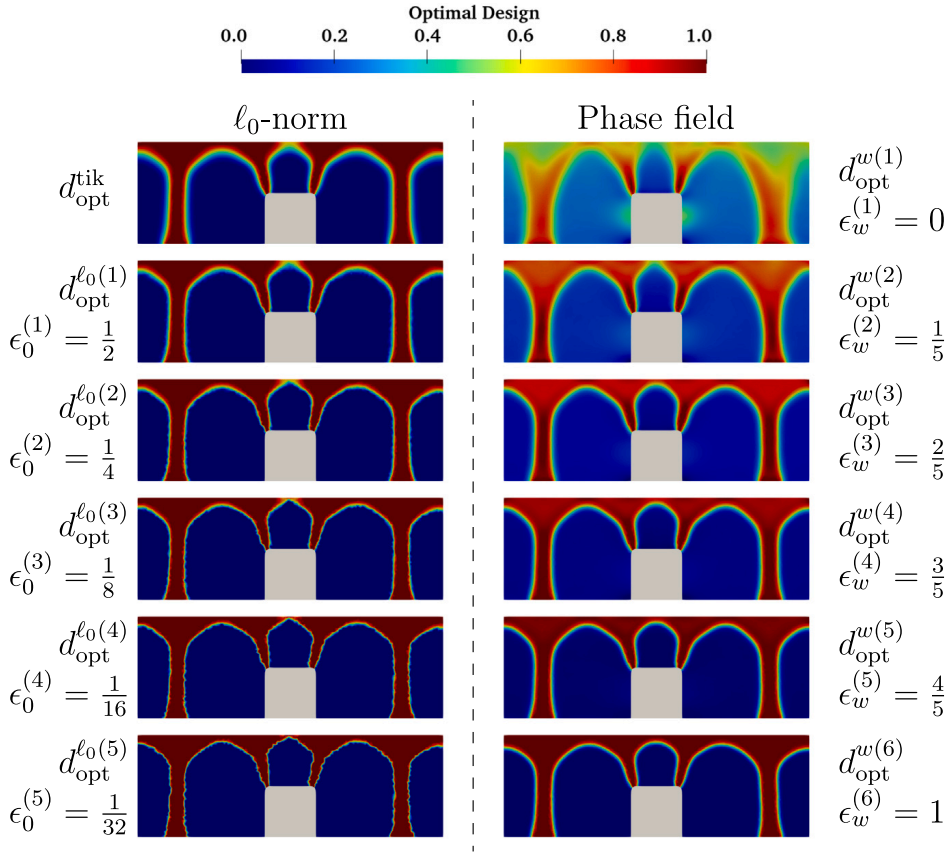

Fig. 15. Optimal design solutions for *Scenario I* obtained through six steps of the continuation schemes. (left column) ℓ_0-norm regularization denoted by $d^{\ell_0(\cdot)}_{\text{opt}}$, (right column) phase field regularization with $\beta_{\text{well}} = 1$ and denoted by $d^{w(\cdot)}_{\text{opt}}$.

To demonstrate the continuation schemes associated with the proposed ℓ_0-norm and phase field regularization functionals in (27) and (29), respectively, we consider *Scenario I* with a Tikhonov weight of $\beta_{\text{tik}} = 1 \times 10^{-3}$ and *Scenario II* with $\beta_{\text{tik}} = 4 \times 10^{-3}$. Fig. 14 shows the optimal design solutions of these scenarios employing only Tikhonov regularization $R = \int_\Omega \beta_{\text{tik}} |\nabla d|^2 \, \mathrm{d}\Omega$ within the optimization (6), denoted as $d^{\text{tik}}_{\text{opt}}(\mathbf{x})$. In scenario I, we observe a moderate interface thickness between the sparse design parameters with $d = 0$ and $d = 1$. In contrast, scenario II, with a more pronounced Tikhonov effect, results in a continuous spectrum of design parameters across the domain, unsuitable for practical high-volume manufacturing.

Fig. 15 shows the optimal design solutions for scenario I using the continuation schemes for ℓ_0-norm and phase field regularization functionals detailed in Section 4.3 In the case of the ℓ_0-norm, the continuation is initiated with $d^{\text{tik}}_{\text{opt}}(\mathbf{x})$ (Fig. 14a), whereas for the phase field, it starts with an initial guess $d^{w(0)}_{\text{opt}} = 0$. The number of continuation steps for phase field regularization is set to $K = 6$, striking a balance between computational cost and convergence. For a fair comparison, the tolerance for ℓ_0-norm

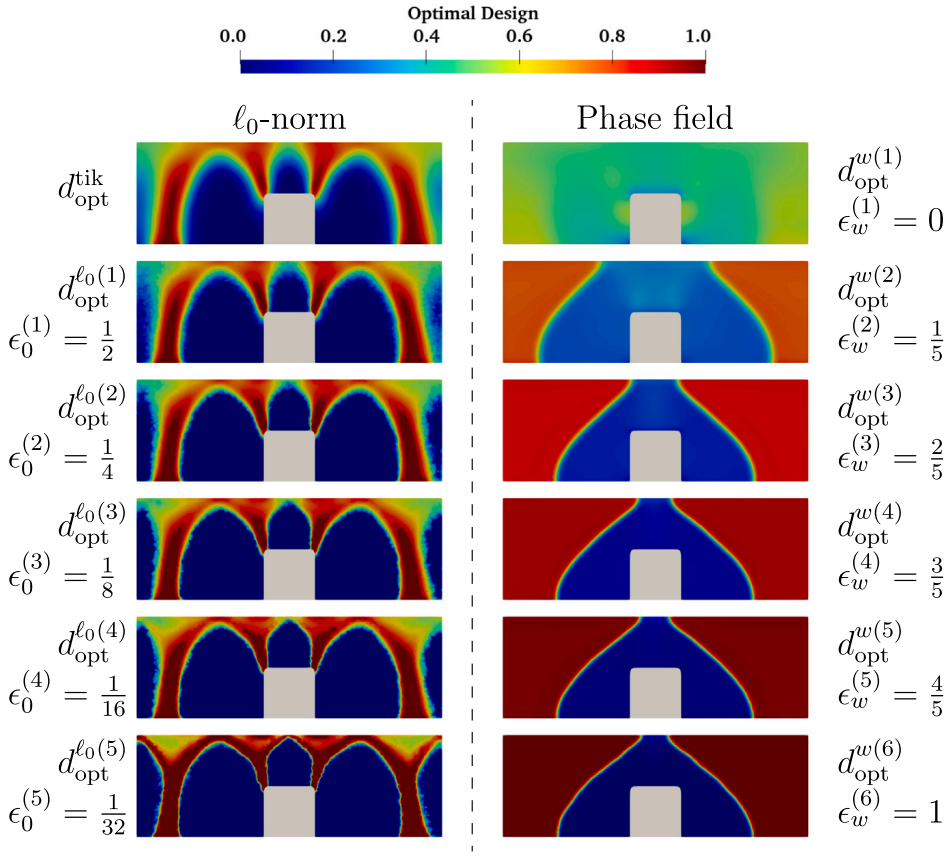

Fig. 16. Optimal design solutions for *Scenario II* obtained through six steps of the continuation schemes. (left column) ℓ_0-norm regularization denoted by $d_{\text{opt}}^{\ell_0(\cdot)}$, (right column) phase field regularization with $\beta_{\text{well}} = 1$ and denoted by $d_{\text{opt}}^{w(\cdot)}$.

regularization is set to 0.03, ensuring that the continuation process concludes with an equivalent number of steps. This figure illustrates that both regularization functionals result in sparsified optimal designs in scenario I. However, the ℓ_0-norm results in a thinner interface thickness, smaller than the resolution resolved by the mesh, compared to the phase field.

The continuation solutions of scenario II are shown in Fig. 16, and the corresponding probability distributions of the design objectives at the optimal designs are shown in Fig. 17. In this scenario, characterized by a higher Tikhonov weight than scenario I, the two regularization techniques produce distinct morphologies for the optimal design parameter. Specifically, in the ℓ_0-norm continuation, the initial design morphology of the Tikhonov solution in Fig. 14 is maintained, with a progressive reduction in interface thickness. In contrast, the phase field continuation forms the overall design morphology into an insulating cloak around the column in the early steps and gradually refines sparsification as the extremum of the double well transitions towards $d = 0, 1$. After an equal number of continuation steps, the phase field regularization attains a fully sparsed solution by compromising the thermal objective, whereas the ℓ_0-norm leads to non-sparse regions. The states and porosities for the mean and samples of the uncertain parameters at the final step of the optimal design process are displayed in Fig. 18 for ℓ_0-norm and Fig. 19 for phase field continuation. These results indicate that the phase field regularization leads to lower stress concentration and higher fluid pressure to attain mechanical stability while leading to weaker insulation performance than the ℓ_0-norm regularized design.

Remarks. Regarding the ℓ_0-norm and phase field regularization functionals, in terms of enforcing sparsity in the design solution and achieving the thermal and mechanical design objectives, we offer the following remarks:

- The proposed ℓ_0 continuation method attains sparsity by gradually transitioning the regularization function towards the true ℓ_0-norm. This process depends on a self-evolving hyperparameter ϵ_0 and imposes a progressive penalty on design values between $d = 0$ to $d = 1$. The continuation scheme can be stopped when the desired interface thickness is reached. Nevertheless, owing to the non-convex nature of the ℓ_0-norm function, the process must initiate with an optimization step that employs a convex regularizer such as Tikhonov. Lastly, the ℓ_0-norm function exhibits a bias towards favoring $d = 0$ when dealing with non-sparse regions during the continuation scheme.
- The proposed phase field continuation achieves sparsity by gradually transforming a convex single well initially centered at $d = 0.5$, transitioning it into a double well with extrema at $d = 0$ and $d = 1$. As a result, all continuation steps must be completed without an early termination option to attain a sparsified solution. Unlike the ℓ_0-norm approach, the convex nature

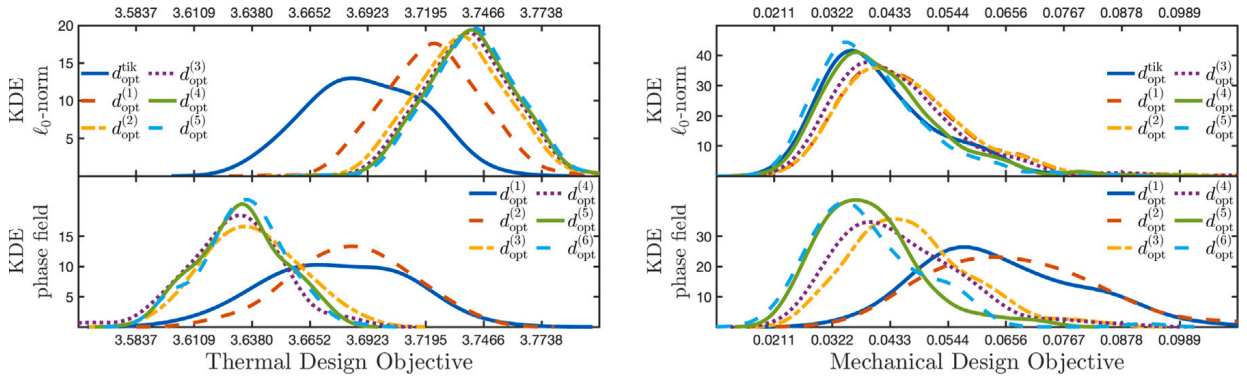

Fig. 17. The probability distributions of thermal Q_T and mechanical Q_M objectives of *Scenario II* at optimal design obtained using ℓ_0-norm $d_{\text{opt}}^{\ell_0(5)}$ and phase field $d_{\text{opt}}^{w(6)}$ corresponding to Fig. 16.

of the phase field functional eliminates the need for an initial optimization step. However, it requires an additional weighting parameter, β_{well}, which implicitly controls the final interface thickness. Lastly, due to the symmetry of the double well, the regularization treats both of its extremums ($d = 0$ and $d = 1$) equally.

- The solution accuracy and computational efficiency of both continuation schemes can be significantly enhanced by seamlessly integrating it with the adaptive refinement strategies of multiple discretizations, e.g., [90,91]. This entails mesh refinement for the design parameter discretization at high gradient regions and coarsening in other areas to accurately capture interface formation between sparse design parameters. Concurrently, individual discretization refinement for each state variable **u** to ensure the accuracy of the forward model solution. The results demonstrating smooth interfaces in the optimal design solution for scenario II through adaptive mesh refinement can be found in [61].

8. Conclusions

This work presents an efficient and scalable computational framework for multi-objective optimal design governed by PDEs and in the presence of high-dimensional uncertainty. The problem of interest is optimizing the spatial distribution of uncertain, spatially correlated material porosity field within building thermal insulation components, aiming to achieve both effective insulation and mechanical stability. The framework employs quadratic Taylor expansions of the design objective with respect to the uncertain parameter to estimate both mean and variance within the cost function. It introduces two regularization techniques based on approximate ℓ_0-norm and phase field to achieve the desired sparse design. The optimization solution includes a randomized algorithm for solving generalized eigenvalue problems, enabling efficient approximation of the trace of the covariance-preconditioned Hessian. Additionally, it implements continuation numerical schemes for implementing the sparsity-enforcing regularizations to achieve globally optimal solutions. The scalability of this framework stems from the rapid decay of the eigenvalues and the dimension-independent number of required optimization iterations. Consequently, the computational cost is governed by the rank of the preconditioned Hessian rather than the dimension of the discretized uncertain parameter field. We implement the proposed PDE-constrained design under uncertainty framework on two examples of insulation components. These numerical experiments demonstrate the efficiency and accuracy of the quadratic approximation compared to Monte Carlo estimations of means and variances, as well as the scalability of the optimization concerning the number of design parameters. Furthermore, the results suggest that phase field regularization is effective in attaining sparsity in optimal designs. However, ℓ_0-norm regularization provides direct control over the interface thickness between different materials and can outperform phase field regularization in achieving the design objective, even though it may not always result in fully sparse solutions.

In the future, we aim to expand upon the proposed design under uncertainty framework introduced in this study by incorporating uncertainty of the forward model parameters, determined from the experimental measurements of aerogel [6] and using Bayesian methods, e.g., [63,92–95]. Although the numerical results presented in this work indicate that the quadratic approximation provides reasonably accurate solutions for optimal design, even with high uncertainty in the porosity field, challenges may arise when dealing with high variance in the model parameters. The accuracy of the proposed framework can be improved by leveraging higher-order Taylor approximations (e.g., cubic) of the design objective or utilizing the quadratic approximation as control variates to accelerate the Monte Carlo estimations, as demonstrated in [31]. Another promising avenue for future research involves reformulating the problem by considering the mechanical stability of the insulation component to mitigate stress concentration. This extension would require adapting the current algorithm to handle PDE-constrained optimizations with inequality chance constraints, similar to the approaches presented in [38,96]. In this context, obtaining a Pareto design set will provide more profound insights into effectively prioritizing the mean and variance objectives. Finally, despite the efficiency of the current framework, its application in large-scale engineering systems poses a significant challenge due to the computational cost of solving numerous PDEs throughout the optimization process. To address this challenge effectively, one promising approach involves harnessing the capabilities of recently developed derivative-informed neural operators [36,97–101] that provide an accurate approximation of the mapping from joint

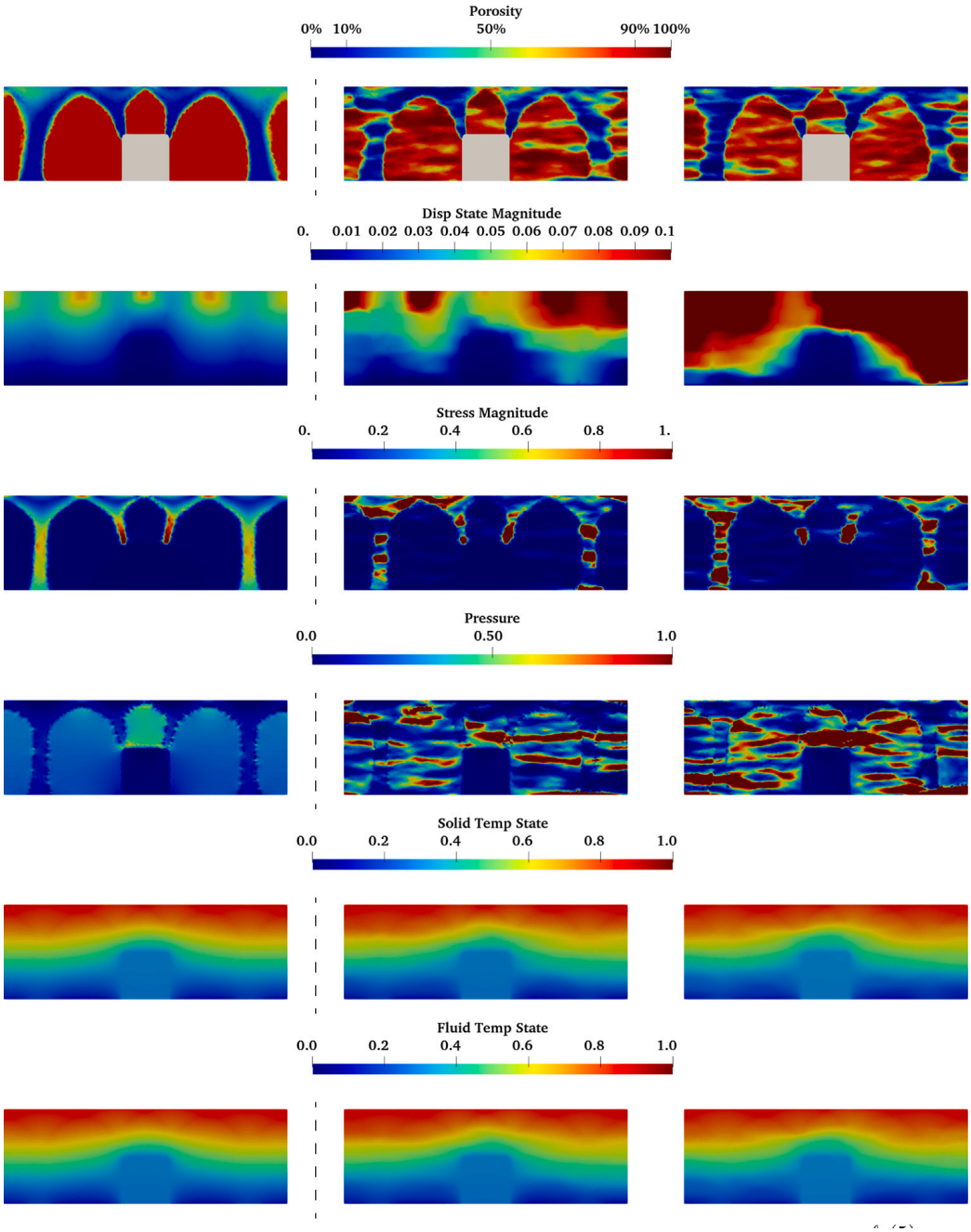

Fig. 18. Porosity and states of *Scenario II* at the optimal design $d^{\ell_0(5)}_{\text{opt}}$ shown in Fig. 16 obtained using (first column) the mean of the uncertain parameter $\bar{m} = 0$, (second and third columns) two i.i.d. samples of m. The rows, respectively, show porosity ϕ_f, magnitude of solid displacement $\|\mathbf{u}_s\|$, magnitude of effective solid stress $\|\mathbf{T}'_s\|$, fluid pressure p, solid temperature θ_s, and fluid temperature θ_f.

uncertain and design parameters to the PDE state and its derivatives with respect to the design parameters. Additionally, this method enables efficient construction of neural networks using reduced basis architectures, ensuring scalability for high-dimensional design problems. An alternative approach to tackle large-scale problems involves harnessing a novel deep learning framework for PDEs solution, as introduced in [102]. This framework involves inferring PDE solutions within a small square domain and progressively assembling them onto larger, arbitrary domains and boundary conditions while maintaining the spatial regularity of the solution. Although the coupling introduces additional complexity, the domain decomposition strategy in this approach significantly reduces the size of the constructed Hessian and can effectively leverage parallel computing to enhance computational efficiency.

In summary, this study emphasizes the critical importance of mitigating uncertainty in ensuring the reliability of optimal design solutions. Our contribution addresses the computational challenges of multi-objective optimization, which involve managing high-dimensional uncertainty and striking a balance between solution sparsity and competing design objectives by incorporating

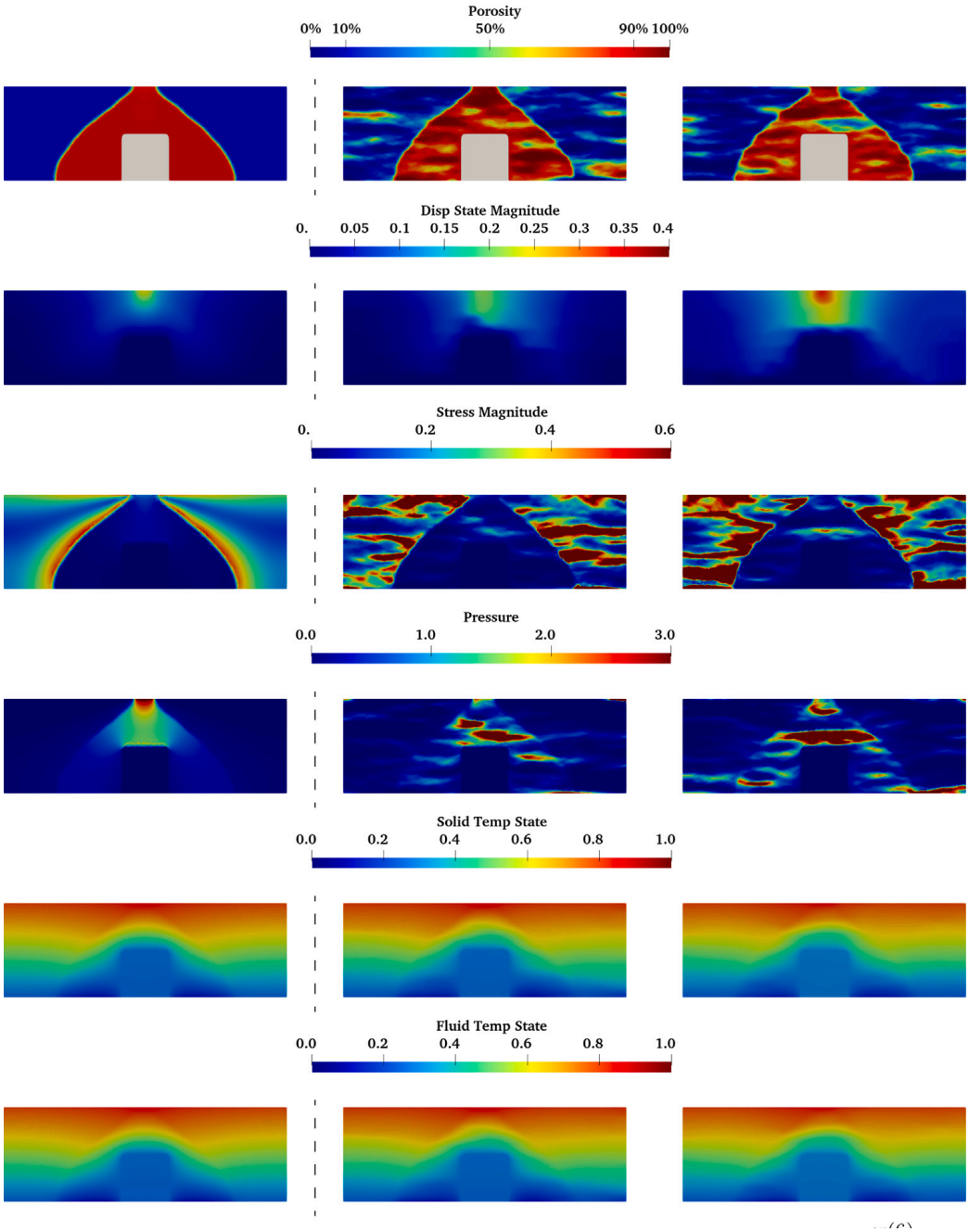

Fig. 19. Porosity and states of *Scenario II* at the optimal design $d_{\text{opt}}^{w(6)}$ shown in Fig. 16 obtained using (first column) the mean of the uncertain parameter $\bar{m} = 0$, (second and third columns) two i.i.d. samples of m. The rows, respectively, show porosity ϕ_f, magnitude of solid displacement $\|\mathbf{u}_s\|$, magnitude of effective solid stress $\|\mathbf{T}'_s\|$, fluid pressure p, solid temperature θ_s, and fluid temperature θ_f.

appropriate regularizations. While this work proposes an effective framework for design under uncertainty, opportunities for further enhancement exist and will be explored in future research works.

Declaration of competing interest

The authors declare the following financial interests/personal relationships which may be considered as potential competing interests: Danial Faghihi and Jingye Tan reports financial support was provided by National Science Foundation (NSF).

Data availability

Data will be made available on request.

Acknowledgments

The authors gratefully acknowledge the financial support received from the U.S. National Science Foundation (NSF) CAREER Award CMMI-2143662. The authors express their appreciation for the helpful discussions with Dr. Umberto Villa, Dr. Lianghao Cao, and Dingcheng Luo, from the University of Texas at Austin, and Dr. Peng Chen, from Georgia Institute of Technology, regarding the problem formulation and software libraries. Their valuable insights and input have been instrumental in shaping this research. Additionally, the authors would like to acknowledge the support provided by the Center for Computational Research at the University at Buffalo.

References

[1] D. Topuzi, Structural thermal breaks, Struct. Des. (2020) URL https://www.structuremag.org/?p=16419.
[2] S. Hamel, K. Peterman, Thermal breaks in building envelopes, Struct. Sustain. (2019) URL https://www.structuremag.org/?p=14102.
[3] R. Yang, F. Hu, L. An, J. Armstrong, Y. Hu, C. Li, Y. Huang, S. Ren, A hierarchical mesoporous insulation ceramic, Nano Lett. 20 (2) (2019) 1110–1116.
[4] L. An, J. Wang, D. Petit, J.N. Armstrong, K. Hanson, J. Hamilton, M. Souza, D. Zhao, C. Li, Y. Liu, et al., An all-ceramic, anisotropic, and flexible aerogel insulation material, Nano Lett. 20 (5) (2020) 3828–3835.
[5] L. An, B. Liang, Z. Guo, J. Wang, C. Li, Y. Huang, Y. Hu, Z. Li, J.N. Armstrong, C. Zhou, et al., Wearable aramid–ceramic aerogel composite for harsh environment, Adv. Eng. Mater. 23 (3) (2021) 2001169.
[6] L. An, M. Di Luigi, J. Tan, D. Faghihi, S. Ren, Flexible percolation fibrous thermal insulating composite membranes for thermal management, Mater. Adv. 4 (1) (2023) 284–290.
[7] T. Gao, B.P. Jelle, A. Gustavsen, J. He, Lightweight and thermally insulating aerogel glass materials, Appl. Phys. A 117 (2) (2014) 799–808.
[8] U. Berardi, The benefits of using aerogel-enhanced systems in building retrofits, Energy Procedia 134 (2017) 626–635.
[9] E. Cuce, P.M. Cuce, C.J. Wood, S.B. Riffat, Toward aerogel based thermal superinsulation in buildings: a comprehensive review, Renew. Sustain. Energy Rev. 34 (2014) 273–299.
[10] Z. Guo, L. An, S. Lakshmanan, J.N. Armstrong, S. Ren, C. Zhou, Additive manufacturing of porous ceramics with foaming agent, J. Manuf. Sci. Eng. 144 (2) (2022) 021010.
[11] Z. Guo, R. Yang, T. Wang, L. An, S. Ren, C. Zhou, Cost-effective additive manufacturing of ambient pressure-dried silica aerogel, J. Manuf. Sci. Eng. 143 (1) (2021).
[12] S. Zhao, G. Siqueira, S. Drdova, D. Norris, C. Ubert, A. Bonnin, S. Galmarini, M. Ganobjak, Z. Pan, S. Brunner, et al., Additive manufacturing of silica aerogels, Nature 584 (7821) (2020) 387–392.
[13] M. Bessa, R. Bostanabad, Z. Liu, A. Hu, D.W. Apley, C. Brinson, W. Chen, W.K. Liu, A framework for data-driven analysis of materials under uncertainty: Countering the curse of dimensionality, Comput. Methods Appl. Mech. Engrg. 320 (2017) 633–667, http://dx.doi.org/10.1016/j.cma.2017.03.037, URL https://www.sciencedirect.com/science/article/pii/S0045782516314803.
[14] W. Chen, A. Iyer, R. Bostanabad, Data centric design: A new approach to design of microstructural material systems, Engineering 10 (2022) 89–98, http://dx.doi.org/10.1016/j.eng.2021.05.022, URL https://www.sciencedirect.com/science/article/pii/S209580992200056X.
[15] S. Ganapathysubramanian, N. Zabaras, Design across length scales: a reduced-order model of polycrystal plasticity for the control of microstructure-sensitive material properties, Comput. Methods Appl. Mech. Engrg. 193 (45) (2004) 5017–5034, http://dx.doi.org/10.1016/j.cma.2004.04.004, URL https://www.sciencedirect.com/science/article/pii/S0045782504002567.
[16] R.E. Christiansen, J. Vester-Petersen, S.P. Madsen, O. Sigmund, A non-linear material interpolation for design of metallic nano-particles using topology optimization, Comput. Methods Appl. Mech. Engrg. 343 (2019) 23–39, http://dx.doi.org/10.1016/j.cma.2018.08.034, URL https://www.sciencedirect.com/science/article/pii/S0045782518304328.
[17] O. Giraldo-Londoño, L. Mirabella, L. Dalloro, G.H. Paulino, Multi-material thermomechanical topology optimization with applications to additive manufacturing: Design of main composite part and its support structure, Comput. Methods Appl. Mech. Engrg. 363 (2020) 112812, http://dx.doi.org/10.1016/j.cma.2019.112812, URL https://www.sciencedirect.com/science/article/pii/S0045782519307042.
[18] H. Zhang, W. Chen, A. Iyer, D.W. Apley, W. Chen, Uncertainty-aware mixed-variable machine learning for materials design, Sci. Rep. 12 (1) (2022) 19760, http://dx.doi.org/10.1038/s41598-022-23431-2.
[19] R. Bostanabad, Y.-C. Chan, L. Wang, P. Zhu, W. Chen, Globally approximate Gaussian processes for big data with application to data-driven metamaterials design, J. Mech. Des. 141 (11) (2019) 111402, http://dx.doi.org/10.1115/1.4044257.
[20] W. Li, F. Wang, O. Sigmund, X.S. Zhang, Design of composite structures with programmable elastic responses under finite deformations, J. Mech. Phys. Solids 151 (2021) 104356.
[21] Z. Zhao, X.S. Zhang, Topology optimization of hard-magnetic soft materials, J. Mech. Phys. Solids 158 (2022) 104628.
[22] R. Bostanabad, Y. Zhang, X. Li, T. Kearney, L.C. Brinson, D.W. Apley, W.K. Liu, W. Chen, Computational microstructure characterization and reconstruction: Review of the state-of-the-art techniques, Prog. Mater. Sci. 95 (2018) 1–41.
[23] R. Bostanabad, A.T. Bui, W. Xie, D.W. Apley, W. Chen, Stochastic microstructure characterization and reconstruction via supervised learning, Acta Mater. 103 (2016) 89–102.
[24] J. Guilleminot, A. Asadpoure, M. Tootkaboni, Topology optimization under topologically dependent material uncertainties, Struct. Multidiscip. Optim. 60 (2019) 1283–1287.
[25] V. Keshavarzzadeh, R.M. Kirby, A. Narayan, Stress-based topology optimization under uncertainty via simulation-based Gaussian process, Comput. Methods Appl. Mech. Engrg. 365 (2020) 112992.
[26] V. Keshavarzzadeh, F. Fernandez, D.A. Tortorelli, Topology optimization under uncertainty via non-intrusive polynomial chaos expansion, Comput. Methods Appl. Mech. Engrg. 318 (2017) 120–147.
[27] S. De, J. Hampton, K. Maute, A. Doostan, Topology optimization under uncertainty using a stochastic gradient-based approach, Struct. Multidiscip. Optim. 62 (2020) 2255–2278.
[28] K. Maute, Topology optimization under uncertainty, in: Topology Optimization in Structural and Continuum Mechanics, Springer, 2014, pp. 457–471.
[29] A. Alexanderian, N. Petra, G. Stadler, O. Ghattas, A-optimal design of experiments for infinite-dimensional Bayesian linear inverse problems with regularized \ell_0-sparsification, SIAM J. Sci. Comput. 36 (5) (2014) A2122–A2148.
[30] A. Alexanderian, N. Petra, G. Stadler, O. Ghattas, Mean-variance risk-averse optimal control of systems governed by PDEs with random parameter fields using quadratic approximations, SIAM/ASA J. Uncertain. Quant. 5 (1) (2017) 1166–1192.
[31] P. Chen, U. Villa, O. Ghattas, Taylor approximation and variance reduction for PDE-constrained optimal control under uncertainty, J. Comput. Phys. 385 (2019) 163–186.
[32] P. Chen, M.R. Haberman, O. Ghattas, Optimal design of acoustic metamaterial cloaks under uncertainty, J. Comput. Phys. 431 (2021) 110114.
[33] L.W. Ng, K.E. Willcox, Multifidelity approaches for optimization under uncertainty, Internat. J. Numer. Methods Engrg. 100 (10) (2014) 746–772.

[34] J. Hyun, A. Chaudhuri, K.E. Willcox, H.A. Kim, Multifidelity robust topology optimization for material uncertainties with digital manufacturing, in: AIAA SCITECH 2023 Forum, 2023, p. 2038.
[35] S. McBane, Y. Choi, K. Willcox, Stress-constrained topology optimization of lattice-like structures using component-wise reduced order models, Comput. Methods Appl. Mech. Engrg. 400 (2022) 115525.
[36] D. Luo, T. O'Leary-Roseberry, P. Chen, O. Ghattas, Efficient PDE-constrained optimization under high-dimensional uncertainty using derivative-informed neural operators, 2023, arXiv preprint arXiv:2305.20053.
[37] D. Luo, L. Cao, P. Chen, O. Ghattas, J.T. Oden, Optimal design of chemoepitaxial guideposts for the directed self-assembly of block copolymer systems using an inexact Newton algorithm, J. Comput. Phys. 485 (2023) 112101.
[38] P. Chen, O. Ghattas, Taylor approximation for chance-constrained optimization problems governed by partial differential equations with high-dimensional random parameters, SIAM/ASA J. Uncertain. Quant. 9 (4) (2021) 1381–1410.
[39] J. Zheng, G. Zhang, C. Jiang, Stress-based topology optimization of thermoelastic structures considering self-support constraints, Comput. Methods Appl. Mech. Engrg. 408 (2023) 115957.
[40] J.C. Krüger, M. Kranz, T. Schmidt, R. Seifried, B. Kriegesmann, An efficient and non-intrusive approach for robust design optimization with the first-order second-moment method, Comput. Methods Appl. Mech. Engrg. 414 (2023) 116136.
[41] Z. Li, L. Wang, Z. Luo, A feature-driven robust topology optimization strategy considering movable non-design domain and complex uncertainty, Comput. Methods Appl. Mech. Engrg. 401 (2022) 115658.
[42] J. Zheng, Z. Luo, C. Jiang, J. Wu, Level-set topology optimization for robust design of structures under hybrid uncertainties, Internat. J. Numer. Methods Engrg. 117 (5) (2019) 523–542.
[43] H. Tiesler, R.M. Kirby, D. Xiu, T. Preusser, Stochastic collocation for optimal control problems with stochastic PDE constraints, SIAM J. Control Optim. 50 (5) (2012) 2659–2682.
[44] E. Rosseel, G.N. Wells, Optimal control with stochastic PDE constraints and uncertain controls, Comput. Methods Appl. Mech. Engrg. 213 (2012) 152–167.
[45] D.P. Kouri, T.M. Surowiec, Risk-averse PDE-constrained optimization using the conditional value-at-risk, SIAM J. Optim. 26 (1) (2016) 365–396.
[46] T. Lassila, A. Manzoni, A. Quarteroni, G. Rozza, Boundary control and shape optimization for the robust design of bypass anastomoses under uncertainty, ESAIM Math. Model. Numer. Anal. 47 (4) (2013) 1107–1131.
[47] R.C. Smith, Uncertainty Quantification: Theory, Implementation, and Applications, Vol. 12, Siam, 2013.
[48] D.G. Cacuci, M. Ionescu-Bujor, I.M. Navon, Sensitivity and Uncertainty Analysis, Volume II: Applications to Large-Scale Systems, Vol. 2, CRC Press, 2005.
[49] I. Doltsinis, Z. Kang, G. Cheng, Robust design of non-linear structures using optimization methods, Comput. Methods Appl. Mech. Engrg. 194 (12–16) (2005) 1779–1795.
[50] I. Doltsinis, Z. Kang, Robust design of structures using optimization methods, Comput. Methods Appl. Mech. Engrg. 193 (23–26) (2004) 2221–2237.
[51] B.S. Lazarov, M. Schevenels, O. Sigmund, Topology optimization with geometric uncertainties by perturbation techniques, Internat. J. Numer. Methods Engrg. 90 (11) (2012) 1321–1336.
[52] M. Kranz, J.K. Lüdeker, B. Kriegesmann, A generalized approach for robust topology optimization using the first-order second-moment method for arbitrary response functions, Struct. Multidiscip. Optim. 66 (5) (2023) 98, http://dx.doi.org/10.1007/s00158-023-03540-w.
[53] B. Kriegesmann, J.K. Lüdeker, Robust compliance topology optimization using the first-order second-moment method, Struct. Multidiscip. Optim. 60 (1) (2019) 269–286, http://dx.doi.org/10.1007/s00158-019-02216-8.
[54] J.C. Krüger, M. Kranz, T. Schmidt, R. Seifried, B. Kriegesmann, An efficient and non-intrusive approach for robust design optimization with the first-order second-moment method, Comput. Methods Appl. Mech. Engrg. 414 (2023) 116136, http://dx.doi.org/10.1016/j.cma.2023.116136, URL https://www.sciencedirect.com/science/article/pii/S0045782523002608.
[55] P. Chen, J.O. Royset, Performance bounds for PDE-constrained optimization under uncertainty, SIAM J. Optim. 33 (3) (2023) 1828–1854.
[56] J. Tan, P. Maleki, L. An, M. Di Luigi, U. Villa, C. Zhou, S. Ren, D. Faghihi, A predictive multiphase model of silica aerogels for building envelope insulations, Comput. Mech. (2022) 1–23.
[57] F. Lindgren, H. Rue, J. Lindström, An explicit link between Gaussian fields and Gaussian Markov random fields: the stochastic partial differential equation approach, J. R. Stat. Soc. Ser. B Stat. Methodol. 73 (4) (2011) 423–498.
[58] L. Roininen, J. Huttunen, S. Lasanen, Whittle-Matérn priors for Bayesian statistical inversion with applications in electrical impedance tomography, Inverse Probl. Imag. 8 (2014) 561–586, http://dx.doi.org/10.3934/ipi.2014.8.561.
[59] Y. Daon, G. Stadler, Mitigating the influence of the boundary on PDE-based covariance operators, Inverse Probl. Imag. 12 (5) (2018) 1083–1102, http://dx.doi.org/10.3934/ipi.2018045.
[60] A. Alexanderian, P.J. Gloor, O. Ghattas, On Bayesian A-and D-optimal experimental designs in infinite dimensions, 2016.
[61] J. Tan, Predictive Modeling and Design of Ceramic Porous Materials Under Uncertainty (Ph.D. thesis), University at Buffalo, State University of New York, 2023.
[62] H. Avron, S. Toledo, Randomized algorithms for estimating the trace of an implicit symmetric positive semi-definite matrix, J. ACM 58 (2) (2011) 1–34.
[63] B. Liang, J. Tan, L. Lozenski, D.A. Hormuth II, T.E. Yankeelov, U. Villa, D. Faghihi, Bayesian inference of tissue heterogeneity for individualized prediction of glioma growth, IEEE Trans. Med. Imaging (2023).
[64] H.P. Flath, L.C. Wilcox, V. Akçelik, J. Hill, B. van Bloemen Waanders, O. Ghattas, Fast algorithms for Bayesian uncertainty quantification in large-scale linear inverse problems based on low-rank partial Hessian approximations, SIAM J. Sci. Comput. 33 (1) (2011) 407–432.
[65] T. Bui-Thanh, O. Ghattas, Analysis of the Hessian for inverse scattering problems: I. Inverse shape scattering of acoustic waves, Inverse Problems 28 (5) (2012) 055001.
[66] O. Bashir, K. Willcox, O. Ghattas, B. van Bloemen Waanders, J. Hill, Hessian-based model reduction for large-scale systems with initial-condition inputs, Internat. J. Numer. Methods Engrg. 73 (6) (2008) 844–868.
[67] A.K. Saibaba, J. Lee, P.K. Kitanidis, Randomized algorithms for generalized Hermitian eigenvalue problems with application to computing Karhunen–Loève expansion, Numer. Linear Algebra Appl. 23 (2) (2016) 314–339.
[68] C. Louizos, M. Welling, D.P. Kingma, Learning sparse neural networks through L_0 regularization, 2017, arXiv preprint arXiv:1712.01312.
[69] D. Faghihi, X. Feng, E.A. Lima, J.T. Oden, T.E. Yankeelov, A coupled mass transport and deformation theory of multi-constituent tumor growth, J. Mech. Phys. Solids 139 (2020) 103936.
[70] P.K. Singh, L. Cao, J. Tan, D. Faghihi, A nonlocal theory of heat transfer and micro-phase separation of nanostructured copolymers, Int. J. Heat Mass Transfer 215 (2023) 124474, http://dx.doi.org/10.1016/j.ijheatmasstransfer.2023.124474, URL https://www.sciencedirect.com/science/article/pii/S0017931023006191.
[71] W. Lu, D. Salac, Patterning multilayers of molecules via self-organization, Phys. Rev. Lett. 94 (14) (2005) 146103.
[72] L. Cao, O. Ghattas, J.T. Oden, A globally convergent modified Newton method for the direct minimization of the Ohta–Kawasaki energy with application to the directed self-assembly of Diblock copolymers, SIAM J. Sci. Comput. 44 (1) (2022) B51–B79.
[73] M. Burger, R. Stainko, Phase-field relaxation of topology optimization with local stress constraints, SIAM J. Control Optim. 45 (4) (2006) 1447–1466.
[74] A. Takezawa, S. Nishiwaki, M. Kitamura, Shape and topology optimization based on the phase field method and sensitivity analysis, J. Comput. Phys. 229 (7) (2010) 2697–2718.
[75] A.L. Gain, G.H. Paulino, Phase-field based topology optimization with polygonal elements: a finite volume approach for the evolution equation, Struct. Multidiscip. Optim. 46 (2012) 327–342.

[76] S.M. Allen, J.W. Cahn, A correction to the ground state of fcc binary ordered alloys with first and second neighbor pairwise interactions, Scr. Metall. 7 (12) (1973) 1261–1264.
[77] S.M. Allen, J.W. Cahn, Ground state structures in ordered binary alloys with second neighbor interactions, Acta Metall. 20 (3) (1972) 423–433.
[78] H. Garcke, K.F. Lam, R. Nürnberg, A. Signori, Phase field topology optimisation for 4D printing, ESAIM Control Optim. Calc. Var. 29 (2023) 24.
[79] J. Nocedal, S.J. Wright, Numerical Optimization, Springer, 1999.
[80] W. Chen, C. Hoyle, H.J. Wassenaar, Decision-Based Design: Integrating Consumer Preferences Into Engineering Design, Springer, 2013.
[81] P.C. Hansen, The L-Curve and Its Use in the Numerical Treatment of Inverse Problems, IMM, Department of Mathematical Modelling, Technical Universityof Denmark, 1999.
[82] O. Scherzer, The use of Morozov's discrepancy principle for Tikhonov regularization for solving nonlinear ill-posed problems, Computing 51 (1) (1993) 45–60.
[83] D. Colton, M. Piana, R. Potthast, A simple method using Morozov's discrepancy principle for solving inverse scattering problems, Inverse Problems 13 (6) (1997) 1477.
[84] S. Pereverzev, E. Schock, Morozov's discrepancy principle for tikhonov, Numer. Funct. Anal. Optim. 21 (7–8) (2000) 901–916.
[85] M.S. Alnæs, J. Blechta, J. Hake, A. Johansson, B. Kehlet, A. Logg, C. Richardson, J. Ring, M.E. Rognes, G.N. Wells, The FEniCS project version 1.5, Arch. Numer. Softw. 3 (100) (2015) http://dx.doi.org/10.11588/ans.2015.100.20553.
[86] U. Villa, N. Petra, O. Ghattas, HIPPYlib: An extensible software framework for large-scale inverse problems governed by PDEs: Part I: Deterministic inversion and linearized Bayesian inference, ACM Trans. Math. Software 47 (2) (2021) http://dx.doi.org/10.1145/3428447.
[87] U. Villa, N. Petra, O. Ghattas, hIPPYlib: an extensible software framework for large-scale deterministic and Bayesian inverse problems, J. Open Source Softw. 3 (30) (2018) http://dx.doi.org/10.21105/joss.00940.
[88] U. Villa, N. Petra, O. Ghattas, hIPPYlib: an extensible software framework for large-scale deterministic and Bayesian inverse problems, 2016, http://dx.doi.org/10.5281/zenodo.596931, URL http://hippylib.github.io.
[89] P. Virtanen, R. Gommers, T.E. Oliphant, M. Haberland, T. Reddy, D. Cournapeau, E. Burovski, P. Peterson, W. Weckesser, J. Bright, S.J. van der Walt, M. Brett, J. Wilson, K.J. Millman, N. Mayorov, A.R.J. Nelson, E. Jones, R. Kern, E. Larson, C.J. Carey, İ. Polat, Y. Feng, E.W. Moore, J. VanderPlas, D. Laxalde, J. Perktold, R. Cimrman, I. Henriksen, E.A. Quintero, C.R. Harris, A.M. Archibald, A.H. Ribeiro, F. Pedregosa, P. van Mulbregt, SciPy 1.0 Contributors, SciPy 1.0: Fundamental algorithms for scientific computing in python, Nature Methods 17 (2020) 261–272, http://dx.doi.org/10.1038/s41592-019-0686-2.
[90] J. Guest, A. Asadpoure, T. Igusa, A multi-mesh strategy for continuum topology optimization under correlated uncertainties, in: 13th AIAA/ISSMO Multidisciplinary Analysis Optimization Conference, 2010, p. 9328.
[91] T.H. Nguyen, G.H. Paulino, J. Song, C.H. Le, Improving multiresolution topology optimization via multiple discretizations, Internat. J. Numer. Methods Engrg. 92 (6) (2012) 507–530.
[92] J. Tan, K. Maupin, S. Shao, D. Faghihi, A Bayesian machine learning framework for selection of the strain gradient plasticity multiscale model, in: ASME International Mechanical Engineering Congress and Exposition, Vol. 85680, American Society of Mechanical Engineers, 2021, V012T12A009.
[93] J.T. Oden, I. Babuška, D. Faghihi, Predictive computational science: Computer predictions in the presence of uncertainty, in: Encyclopedia of Computational Mechanics Second Edition, Wiley Online Library, 2017, pp. 1–26.
[94] K. Farrell, J.T. Oden, D. Faghihi, A Bayesian framework for adaptive selection, calibration, and validation of coarse-grained models of atomistic systems, J. Comput. Phys. 295 (2015) 189–208.
[95] J. Tan, U. Villa, N. Shamsaei, S. Shao, H.M. Zbib, D. Faghihi, A predictive discrete-continuum multiscale model of plasticity with quantified uncertainty, Int. J. Plast. 138 (2021) 102935.
[96] M.H. Farshbaf-Shaker, R. Henrion, D. Hömberg, Properties of chance constraints in infinite dimensions with an application to PDE constrained optimization, Set-Valued Var. Anal. 26 (2018) 821–841.
[97] L. Cao, T. O'Leary-Roseberry, P.K. Jha, J.T. Oden, O. Ghattas, Residual-based error correction for neural operator accelerated infinite-dimensional Bayesian inverse problems, J. Comput. Phys. 486 (2023) 112104.
[98] K. Wu, T. O'Leary-Roseberry, P. Chen, O. Ghattas, Large-scale Bayesian optimal experimental design with derivative-informed projected neural network, J. Sci. Comput. 95 (1) (2023) 30.
[99] T. O'Leary-Roseberry, X. Du, A. Chaudhuri, J.R. Martins, K. Willcox, O. Ghattas, Learning high-dimensional parametric maps via reduced basis adaptive residual networks, Comput. Methods Appl. Mech. Engrg. 402 (2022) 115730.
[100] T. O'Leary-Roseberry, U. Villa, hippyflow: Dimension Reduced Surrogate Construction for Parametric PDE Maps in Python, Vol. 4608729, 2021, http://dx.doi.org/10.5281/zenodo.
[101] T. O'Leary-Roseberry, U. Villa, P. Chen, O. Ghattas, Derivative-informed projected neural networks for high-dimensional parametric maps governed by PDEs, Comput. Methods Appl. Mech. Engrg. 388 (2022) 114199.
[102] H. Wang, R. Planas, A. Chandramowlishwaran, R. Bostanabad, Mosaic flows: A transferable deep learning framework for solving PDEs on unseen domains, Comput. Methods Appl. Mech. Engrg. 389 (2022) 114424.